# Chapter 12
# Roles and Properties of Cocatalysts in Semiconductor-Based Materials for Efficient $CO_2$ Photoreduction


## 12.1 Introduction

Since the industrial revolution, the rapid development of the economy resulting in the emission amount of $CO_2$ to the atmosphere increased year by year. As a greenhouse gas, $CO_2$ could adsorb the solar energy and raise the temperature itself. Consequently, the excessive $CO_2$ emission would cause global warming and lead to serious environmental problems such as ice mountain melting, sea level rise, ecological balance break, etc., which have gain great attention from the whole world [1]. Recently, the Intergovernmental Panel on Climate Change (IPCC) reports that currently global warming has raised the average temperature of 1.5 °C compared with the preindustrial level [2]; no wonder, it is urgent for us to find possible solutions to cope with the $CO_2$ excessive emission problem. Therefore, the efficient capture and storage of $CO_2$ to further transform it into desirable chemicals with renewable energy input could address the above problems ideally.

Since Fujishima and Honda observed the $H_2$ production by $TiO_2$ electrode under light irradiation [3], semiconductor-based photocatalysts and its applications in environment management and energy transformation have gained much attention [4]. Some reported semiconductors like $TiO_2$, $C_3N_4$, CdS, etc.. possessed suitable bandgaps and reduction potentials which can trigger the $CO_2$ photoreduction reaction (CO2PR) with $H_2O$. However, as a very stable molecule, $CO_2$ photoreduction with $H_2O$ is difficult to occur, owing to this process involved with multiple steps like breaking the C=O bonds and forming the C-H bonds, which both are endothermic reactions and also required abundant electrons and corresponding H protons. In addition, as a major competing reaction, $H_2O$ reduction to $H_2$ is more easily to occur in both thermodynamics and kinetics [5–7]. In this way, bare semiconductors without modification often show low $CO_2$ photoreduction activity and selectivity.

In the use of semiconductor as the photocatalyst to trigger $CO_2$ conversion with $H_2O$, the activity is mainly affected by three key factors: (i) light adsorption and the excitation of semiconductors, (ii) photo-generated electron-hole pairs' separation



J. Zhang et al., *Photocatalysis*, Lecture Notes in Chemistry 100,
https://doi.org/10.1007/978-981-13-2113-9_12

and transfer, and (iii) surface catalytic reactions. Based on these principles, semiconductors modified with suitable cocatalysts can greatly boost the CO2PR activity and selectivity [4, 8]. In Table 12.1 we summarized the semiconductor-based photocatalysts with various cocatalysts loaded in CO2PR based on the researches in recent years. The content of Table 12.1 including the optimal products (such as $CH_4$, CO, $CH_3OH$, HCOOH, and $H_2$) yields brief introduction of photocatalysts' preparation, CO2PR evaluation details, etc. Among these cocatalysts, for example, noble metal NPs like Pt [8–13], Au [14], Pd [15–18], Ag [19–21], etc., lower Fermi level is often considered as efficient cocatalysts for electron trapping and active site with suitable binding energy to some intermediates [5]; combined semiconductors with suitable band structures together can form p–n junction or Z-scheme and thus favored the light adsorption and charge separation [22–25]; the semiconductor–MOF or semiconductor–graphene composites often show enhanced $CO_2$ adsorption performance and effective $CO_2$ activation properties, etc.

In this chapter, we plan to present a short review to discuss about the cocatalysts including metal NPs, metal alloy NPs, graphene, carbon nanodots, MOFs, semiconductors, etc., synthesis methods, and basic roles in $CO_2$ photoreduction based on recent research progress. The advanced techniques such as time-resolved DRIFTS, time-resolved PL decay, EPR, and DFT calculations applied to clarify the charge transfer mechanism and surface catalytic reaction pathways are also discussed in detail.

## 12.2 Basic Principles of $CO_2$ Photoreduction

Generally, semiconductors can be excited by photon carriers with energy higher than its bandgap energy; after the excitation, the photo-generated electron-hole pairs would migrate to the surface for certain reduction/oxidation reactions or recombine together and release energy by means of heat. In order to catalyze the CO2PR reaction with $H_2O$, the photo-generated electron-hole pairs must possess suitable reduction and oxidation potential (Fig. 12.1). According to previous reports, different standard reduction potentials of $CO_2$ reduction with H protons to yield different products are shown in Eqs. 12.1, 12.2, 12.3, 12.4, and 12.5 [5, 26].

$$CO_2 + 2H^+ + 2e^- \rightarrow HCOOH \qquad E_{redox}{}^0 = -0.61V \tag{12.1}$$

$$CO_2 + 2H^+ + 2e^- \rightarrow CO \qquad E_{redox}{}^0 = -0.53V \tag{12.2}$$

$$CO_2 + 6H^+ + 6e^- \rightarrow CH_3OH + H_2O \qquad E_{redox}{}^0 = -0.38V \tag{12.3}$$

$$CO_2 + 8H^+ + 8e^- \rightarrow CH_4 + 4H_2O \qquad E_{redox}{}^0 = -0.24V \tag{12.4}$$

$$CO_2 + e^- \rightarrow CO_2{}^- \qquad E_{redox}{}^0 = -1.90V \tag{12.5}$$

**Table 12.1** Semiconductor-based photocatalysts with cocatalysts in $CO_2$ photoreduction

| | Photocatalysts | Cocatalysts | Optimal product yield (μmol/g·h exception unit stated otherwise) | Brief photocatalyst preparation method | $CO_2$ photoreduction evaluation details | Refs. |
|---|---|---|---|---|---|---|
| 1 | MgO–Pt–$TiO_2$ | MgO, Pt | $CH_4$ (8.9); $H_2$ (8.4) | Impregnation method for MgO modification and photo-deposition for Pt load | 20 mg catalyst placed on a Teflon holder, 0.2 MPa $CO_2$ and 4 mL $H_2O$, temperature was kept at 323 K, 100 W Xe lamp: 60 mW/cm$^2$ at UV range was used as the light source | [10] |
| 2 | Pt–$TiO_2$ single crystal | Pt | $CH_4$ (1361) | tilted-target sputtering (TTS) configuration | Catalyst film, $CO_2$ and $H_2O$ vapor, 400 W Xe lamp was used as the light source, continuous flow | [9] |
| 3 | Pd/$C_3N_4$ | Pd | CO (20.3); $H_2$ (9.7); $CH_4$ (0.28); $C_2H_5OH$ (2.2) | Solution-phase method using different facet-selective capping agents and PVP as reductant and stabilizer | 10 mg catalyst dispersed on a porous holder made of quartz sand, 0.15 MPa $CO_2$ and 3 mL $H_2O$, 300 W Xe lamp with 400 nm cutoff filter: 100 mW/cm$^2$ was used as the light source | [15] |
| 4 | Pd/$TiO_2$ sheet | Pd | CO (12.6); $CH_4$ (3.0) | Self-assembly of pre-synthesized Pd nanosheets onto the $TiO_2$ nanosheets | 10 mg catalyst dispersed on a porous holder made of quartz sand, 0.15 MPa $CO_2$ and 3 mL $H_2O$, 300 W Xe lamp with 400 nm cutoff filter: 100 mW/cm$^2$ was used as the light source | [16] |
| 5 | Ag/Brookite nanocube | Ag | $CH_4$ (11.5); CO (128.8) | $AgNO_3$ was mixed with brookite and reduced by $NaBH_4$ | 0.15 g catalyst, 28 cm$^2$, $CO_2$, and $H_2O$ vapor generate from $NaHCO_3$ + $H_2SO_4$; 300 W Xe lamp was used as the light source | [21] |
| 6 | Metal NPs/$TiO_2$ nanotube | Au, Ru, ZnPd | $CH_4$ (58.47, 26.37, 26.83, respectively) | Stepwise impregnation(colloid synthesis first) of metal NPs | Stainless steel reaction chamber with water droplets, solar simulator equipped with class A filters | [28] |

(continued)

**Table 12.1** (continued)

| | Photocatalysts | Cocatalysts | Optimal product yield (μmol/g·h exception unit stated otherwise) | Brief photocatalyst preparation method | $CO_2$ photoreduction evaluation details | Refs. |
|---|---|---|---|---|---|---|
| 7 | Pt-CdS-$Cu_2S$ | Pt | CO (3.02) | Site-selective growth of Pt on the CdS tips followed by light-induced cation exchange of CdS to $Cu_2S$ | Pt-CdS, 0.1 M $Na_2SO_3$ as hole scavenger, 1 M $Na_2CO_3$ as $CO_2$ source, and 0.63 mM $CuCl_2$ as copper precursor; pH = 11; 450 W Xe lamp was used as the light source | [12] |
| 8 | $Ru/NaTaO_3$ | Ru | $CH_4$ (51.8) | Photo-deposition of Ru on $NaTaO_3$ | 0.07 g sample was loaded in the reactor, 3 mL $H_2O$, 40 kPa $CO_2$, and 40 kPa $H_2$; 300 W Xe lamp was used as the light source | [29] |
| 9 | $Ag/TiO_2$ | Ag | $CH_4$ (1.40) | Silver mirror method by using HCHO and $AgNO_3$ | 0.1 g catalyst-4.2$cm^2$, 0.4 mL $H_2O$, $CO_2$ and $H_2O$ vapor; the system was placed in the dark for 10 h before the light irradiation; 300 W Xe lamp was used as the light source | [30] |
| 10 | $V_o$ (oxygen vacancies)-rich $Pt/Ga_2O_3$ | Pt | CO (105); $CH_4$ (4.75) | Photo-deposition of Pt on $Ga_2O_3$ | 200 mg catalyst dispersed in 100 mL $H_2O$, closed gas circulation–evacuation reactor, 1.01 bar $CO_2$; 300 W Xe lamp was used as the light source | [31] |
| 11 | $Pd/TiO_2$ | Pd | $CH_4$ (118.54); CO (15.45); $H_2$ (13.23) average of 3 h | $Na_2PdCl_4$ was mixed with $TiO_2$ and reduced by glucose | 0.1 g catalyst dispersed onto 0.1 g silica wool in a miniature visual autoclave,150w Hg lamp was used as the light source, 2.5 MPa $H_2$/$CO_2$ = 4:1 | [17] |
| 12 | $Pd_7Cu_1$ alloy-$TiO_2$ | $Pd_7Cu_1$ alloy | $CH_4$ (19.6) | Liquid phase synthesis using $K_2PdCl_4$ and $CuCl_2$ as precursor | 5 mg catalyst mounted above a small quartz beaker placed in a quartz tube, 0.2 Mpa $CO_2$ and 1 mL $H_2O$, 300 W Xe lamp was used as the light source | [18] |

| | | | | | | |
|---|---|---|---|---|---|---|
| 13 | CuPt–$TiO_2$ | Cu-Pt alloy | $CH_4$ (11.3) | Varied Pt and Cu precursor mixed with $TiO_2$ then anneal at air and $H_2$ at 673 K | 1 $cm^2$ 0.4 mg catalyst film placed vertically in reaction chamber with 50uL $H_2O$ and 1.2 atm $CO_2$, 150 W Xe lamp was used as the light source | [32] |
| 14 | Au–Cu/$TiO_2$ (p25) | Au–Cu alloy | $CH_4$ (2200); $H_2$ (286) | Stepwise deposition–precipitation for each metal and then reduced in $H_2$ flow | 0.6 mg catalyst, 1.25 $cm^2$ film, 1.7 atm $H_2O$ saturated $CO_2$ | [14] |
| 15 | Au–Cu@$SrTiO_3$/$TiO_2$ | Au–Cu alloy | $CH_4$ (421.2); CO (3770) | Microwave-assisted solvothermal method | 5 mg catalyst-2.5 $cm^2$, $CO_2$ saturated $N_2H_4$ and $CO_2$; 300 W Xe lamp was used as the light source | [33] |
| 16 | ZnO@$Co_3O_4$ | $Co_3O_4$ | $CH_4$ (0.99) | Synthesize ZIF-8@ZIF-67 first, then followed by annealing treatment at $N_2$ and air, respectively | 0.1 g sample deposited in reaction cell; 3 mL $H_2O$ and 80 kPa $CO_2$ were introduced into the reactor; 300 W Xe lamp was used as the light source | [34] |
| 17 | ZnO-CuO nanowire | ZnO | CO (1.98 mmol/g·h) | Atomic layer deposition(ALD) of ZnO on CuO nanowire | Catalyst film, $CO_2$ passed through a water bubbler to generate $CO_2$ and $H_2O$ mixture, 400 W Xe lamp: 300 mW/$cm^2$ was used as the light source, continuous flow reactor | [35] |
| 18 | g-$C_3N_4$/ZnO | ZnO | $CH_3OH$ (0.6) | Mixing urea and zinc nitrate hexahydrate first then followed by one-step facile calcination method | 100 mg sample was deposited onto the bottom of 200 mL reactor, 0.12 g $NaHCO_3$ and 0.25 mL-4 M HCl was introduced into the reactor as the $CO_2$ and $H_2O$ source, 300 W Xe lamp was used as the light source | [36] |
| 19 | Hybrid CuO–$TiO_{2-x}N_x$ hollow nanocubes | $Cu_2O$ | $CH_4$ (41.3) | Calcination of $TiO_2$@$Cu_3N$ nanotubes as described in the paper | 100 mg catalyst in a reaction chamber, $CO_2$/$H_2O$ mixture, 300 W Xe lamp: 100 mW/$cm^2$ was used as the light source | [37] |

(continued)

**Table 12.1** (continued)

| | Photocatalysts | Cocatalysts | Optimal product yield (μmol/g·h exception unit stated otherwise) | Brief photocatalyst preparation method | $CO_2$ photoreduction evaluation details | Refs. |
|---|---|---|---|---|---|---|
| 20 | Hierarchical Z-scheme CdS–$WO_3$ | CdS | $CH_4$ (1.02) | Deposition precipitation method using $Cd(NO_3)_2$ as precursor and $Na_2S$ as precipitant | 100 mg catalyst added to 10 mL distilled water in a glass reactor, 1 atm $CO_2$, 300 W Xe lamp:150 mW $cm^{-2}$ was used as the light source, ambient temperature | [38] |
| 21 | Z-scheme BiOI/g-$C_3N_4$ | BiOI | CO (4.86); $CH_4$ (0.18); $O_2$ (2.78) | Deposition method using $Bi(NO_3)$ as precursor and KI as precipitant | 0.10 g catalyst, $CO_2$ and $H_2O$ vapor, 300 W Xe lamp with a UV-cutoff flitter ($\lambda > 400$ nm) was used as the light source | [39] |
| 22 | Pt-$MnO_x$/$CeO_2$ | Pt, $MnO_x$ | $CH_4$ (1.12) | One-step photo-deposition method | 0.1 g catalyst-4.2 $cm^2$, 0.4 mL $H_2O$, $CO_2$ and $H_2O$ vapor, the system was placed in dark to reach adsorption-desorption equilibrium before the light irradiation; 300 W Xe lamp was used as the light source | [40] |
| 23 | Pt/HCTSO | Pt, $CoO_x$ | $CH_4$ (9.3); CO (0.3); $H_2$ (14.1) | "EISA" method for co-species incorporation and alcohol reduction for Pt loading | 30 mg filmlike catalyst on 6 $cm^2$ diameter Petri dish, $CO_2$, and 1 mL $H_2O$; 300 W Xe lamp was used as the light source | [8] |
| 24 | Pt@$CuO_x$/$TiO_2$ (p25) | Pt@$CuO_x$ | $CH_4$ (33); CO (8.3); $H_2$ (25) | Stepwise photo-deposition of Pt and $CuO_x$ using a 300 W Hg lamp | 0.02 g catalyst, 0.2 MPa $CO_2$, 4 mL $H_2O$, 200 W Xe lamp was used as the light source | [41] |
| 25 | Pt-$RuO_2$/$Zn_2GeO_4$ nanobelt | Pt, $RuO_2$ | $CH_4$ (25) first hour | Photoreduction of $H_2PtCl_4$ under a 300 W Xe lamp | 0.1 g catalyst-4.2$cm^2$, 1 atm, 1 mL $H_2O$, $CO_2$ and $H_2O$ vapor, 300 W Xe lamp was used as the light source | [42] |

| | | | | | | |
|---|---|---|---|---|---|---|
| 26 | CdSe–Pt–$TiO_2$ | CdSe, Pt, Pd | $CH_3OH$ (90.22 ppm/g.h); $HCOOCH_3$ (225.4 ppm/g.h) | Wet impregnation method for Pd or Pt loading; adding commercial CdSe QDs to $TiO_2$ then anneal in $N_2$ | Stainless steel reaction chamber with 100–140 mg catalyst; $CO_2$ passes through a water bubbler (25 °C) and then enters the reactor; 6 W UV-B lamp with 2 mW/cm$^2$ was used as the light source | [43] |
| 27 | Pt@CdS/inverse opal $TiO_2$ | Pt@CdS | $CH_4$ (36.8) | Gas bubbling-assisted membrane reduction-precipitation (GBMR/P) method | 20 mg catalyst spin coating in 6.5 cm diameter reactor, $CO_2$ and $H_2O$, 300 W Xe lamp: 100 mW/cm$^2$ was used as the light source | [44] |
| 28 | Au@CdS/inverse opal $TiO_2$ | Au@CdS | $CH_4$ (41.6) | Gas bubbling-assisted membrane reduction-precipitation (GBMR/P) method | 20 mg catalyst spin coating in 6.5 cm diameter reactor, $CO_2$ and $H_2O$, 300 W Xe lamp: 100 mW/cm$^2$ was used as the light source | [22] |
| 29 | Z-scheme $Ag_3PO_4$/g-$C_3N_4$ | Ag, $AgPO_4$ | CO (~45); $CH_3OH$ (~10) | In situ deposition of $Ag^+$ using $Na_2HPO_4$ as precipitant | 10 mg catalyst placed in a stainless steel reactor (volume~132 mL), $CO_2$, and 4 mL $H_2O$; 500 W Xe lamp was used as the light source | [25] |
| 30 | Z-scheme $WO_3$/Au/$In_2S_3$ nanowire arrays | $In_2S_3$, Au | $CH_4$ (0.42) | Plasma sputtering method used for loading Au to $WO_3$ and thermal growth for $In_2S_3$ to coat on Au surface | 10 cm$^2$ sample placed on the bottom of a Pyrex glass reactor, ambient pressure $CO_2$, 0.4 mL $H_2O$; 300 W Xe lamp with a UV cutoff filter ($\lambda > 420$ nm) was used as the light source | [45] |
| 31 | Cu-loaded graphene oxide–$TiO_2$ composite | Cu(I) species | $C_2H_5OH$ (144.7 at pH 11.0); $CH_3OH$ (47.0 at pH 4.0) | Add the Cu species to the precursor of graphene oxide-$TiO_2$ followed with thermal treat | 250 mg catalyst dispersed in 250 mL solutions of different pH in a tube photoreactor, UV–vis Heraeus TQ 150 medium-pressure mercury vapor lamp, 27 cm$^3$ min$^{-1}$ he and 3 cm$^3$ min$^{-1}$ $CO_2$, 25 °C | [46] |

(continued)

**Table 12.1** (continued)

| | Photocatalysts | Cocatalysts | Optimal product yield (μmol/g·h exception unit stated otherwise) | Brief photocatalyst preparation method | $CO_2$ photoreduction evaluation details | Refs. |
|---|---|---|---|---|---|---|
| 32 | Pt/carbon-coated $In_2O_3$ nanobelt | Pt, C | CO (126.6); $CH_4$ (27.9) | Hydrothermal synthesis for carbon layer using glucose as precursor and photo-deposition method for depositing Pt from $H_2PtCl_4$ | 200 mg catalyst dispersed in a water solution (200 mL) with 10 vol% triethanolamine placed in a closed gas circulation–evacuation reactor, 1.01 bar $CO_2$; 300 W Xe lamp was used as the light source, 25 °C | [47] |
| 33 | C/H-g-$C_3N_4$ | C | CO (22.6); $CH_4$ (12.5) in 9 h | One-step pyrolysis method using melamine and natural soybean oil as precursors | 0.1 g catalyst in stainless steel reactor, $CO_2$ and $H_2O$ mixture; 500 W Xe lamp was used as the light source, temperature was kept at 303 K, and pressure was maintained at 110 KPa | [48] |
| 34 | $TiO_2$/graphene sandwich structure | Graphene | $CH_4$ (8); $C_2H_6$ (16.8) | One-step hydrothermal method | 0.1 g catalyst placed on a glass reactor with 4.2 $cm^2$ area, $CO_2$ and 1 mL $H_2O$; 300 W Xe lamp was used as the light source | [49] |
| 35 | G-$Ti_{0.91}O_2$ hollow sphere | Graphene | $CH_4$ (1.14); CO (8.91) | The LBL self-assembly approach using GO nanosheets and $Ti_{0.91}O_2$ nanosheets as inorganic shell building blocks | 0.1 g catalyst placed on a glass reactor with 4.2 $cm^2$ area, $CO_2$ and 1 mL $H_2O$; 300 W Xe lamp was used as the light source | [50] |
| 36 | $Co_3O_4$ hexagonal platelets | $[Ru(bpy)_3]Cl_2$ | CO (3523) | $Co_3O_4$ hexagonal platelets was obtained by calcinate β-$Co(OH)_2$ at 400 °C, commercial $[Ru(bpy)_3]Cl_2$ | 10 mg $Co_3O_4$ platelets and 10 mg $[Ru(bpy)_3]Cl_2.6H_2O$, 30 mL solvent (MeCN/TEOA/$H_2O$ = 3:1:1 vol/vol); $CO_2$ 1 bar, 300 W Xe lamp with 420 filter (293.61 mW/$cm^2$) was used as the light source | [51] |

| | | | | | | |
|---|---|---|---|---|---|---|
| 37 | $CsPbBr_3$ perovskite quantum dot/graphene oxide | Graphene oxide | CO (58.7); $CH_4$ (28.6); $H_2$ (1.58) | Modified Hummers' method for GO preparation and then GO–DMF solution was used to synthesize $CsPbBr_3$ QD/GO composite | 4 mg catalyst, 10 mL ethyl acetate, $CO_2$, 100 W Xe lamp with an AM 1.5G filter for simulating solar light: 150 mW/cm$^2$ was used as the light source | [52] |
| 38 | $Cu_3(BTC)_2$@$TiO_2$ | $Cu_3(BTC)_2$<br>BTC is benzene-1,3,5-tricarboxylate | $CH_4$ (2.64 μmol/g-$TiO_2$. h) | Synthesize $Cu_3(BTC)_2$ first then coating $TiO_2$ shell using hydrothermal method. | 100 mL quartz tube reactor; 300 mg $Cu_3(BTC)_2$@$TiO_2$ was placed on quartz boat containing 5 ml $H_2O$, 0.15 MPa $CO_2$; and 300 W Xe lamp was used as the light source | [53] |
| 39 | Reduced graphene oxide-CdS nanorod | Reduced graphene oxide | $CH_4$ (2.51) | Modified Hummers' method for GO preparation, microwave-solvothermal method for rGO-CdS nanorod synthesis | 100 mg sample was deposited onto the bottom of 200 mL reactor, 0.12 g $NaHCO_3$ and 0.25 mL-4 M HCl was introduced into the reactor as the $CO_2$ and $H_2O$ source, 300 W Xe lamp with UV-cutoff ($\lambda > 420$ nm) was used as the light source | [54] |
| 40 | CND/pCN | Carbon nanodots | $CH_4$ (29.23); CO (58.82) | Alkali-assisted ultrasonication method to prepare CNDs first and then mixing CNDs and pCN and followed by hydrothermal treatment | 50 mg sample fixed into quartz tube, $CO_2$ passed through a water bubbler to generate $CO_2$ and $H_2O$ mixture, 1 atm and ambient temperature; 500 W Xe lamp was used as the light source | [55] |
| 41 | Uio-66/$C_3N_4$ nanosheet | Uio-66 | CO (9.9) | $C_3N_4$ nanosheet was obtained by liquid exfoliating bulk $C_3N_4$ in water and then the $C_3N_4$ nanosheet self-assemble with Uio-66 in water | The photocatalyst was dispersed in the reactor cell with 5 mL (MeCN/TEOA = 4:1) solution, after evacuation, 80 kPa CO2 was injected into the system, a 300 W Xe lamp with two filters ($400 < \lambda < 800$ nm) was used as the light source | [56] |

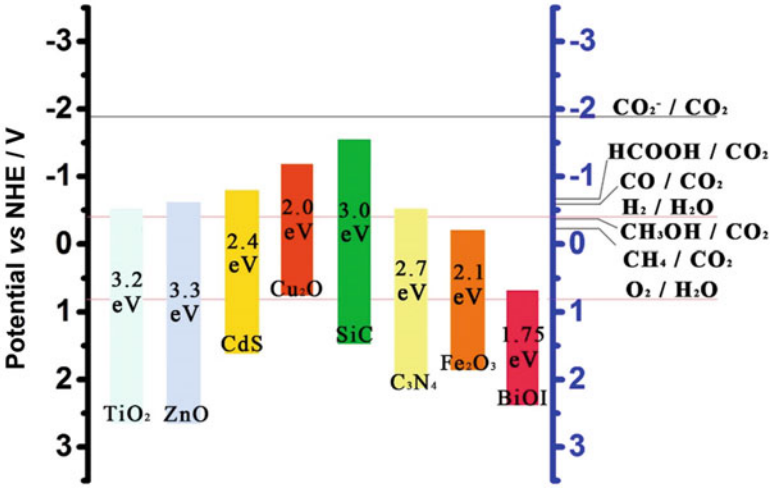


**Fig. 12.1** Band structures of several common semiconductors and corresponding standard reduction potential involved with $CO_2$ and $H_2O$ photocatalytic reduction at pH =7

In most semiconductor-based CO2PR reactions, $H_2O$ is selected as the sole electron donor, in this case, the $H_2O$ oxidation reaction to release H protons and $O_2$; hydrogen evolution reaction (HER) to generate $H_2$ has also two major steps: Eqs. 12.6 and 12.7:

$$2H_2O + 4h^+ \rightarrow 4H^+ + O_2 \qquad E_{redox}{}^0 = -0.82V \qquad (12.6)$$

$$2H^+ + 2e^- \rightarrow H_2 \qquad E_{redox}{}^0 = -0.41V \qquad (12.7)$$

Owing to the complexity of $CO_2$ reduction reaction that involved multi-electrons and protons' participation and various intermediates' adsorption/desorption processes, the deep understanding of the $CO_2$ reduction is still unclear both experimentally and theoretically. To date, researchers have proposed two classic $CO_2$ reduction pathways which are called formaldehyde pathway (also known as multiple proton-coupled electron transfer) and carbene pathway (also known as deoxygenation path), respectively [5, 27]. However, the carbene pathway is initially involved with one electron's $CO_2$ reduction to generate $CO_2^-$ (Eq. 12.5) which cannot be accomplished by many semiconductors owing to the limited reduction potential (Fig. 12.1) [5, 26]. Recently, Ji et al. [27] using $TiO_2$ (101) as the prototype proposed a new mechanism which involved $CO_2$ photoreduction at Ti site and oxygen vacancy site based on DFT calculation. Their result shows that the O vacancy ($O_v$) served as the active site to bind the intermediates like $CH_2O$ or $CH_3O$ and facilitate the $CH_4$ or $CH_3OH$ generation; besides, the $O_v$ also offers two electrons to protect the intermediates from reoxidation. Meanwhile, the intermediates adsorbed on Ti site could be oxidized by holes rapidly and result in low $CO_2$ photoreduction efficiency. Still, considering the alternative catalytic conditions among different

photocatalysts, the study of the reaction mechanism of CO2PR remains challengeable.

## 12.3 Cocatalysts in Semiconductor-Based $CO_2$ Photoreduction

### *12.3.1 Preparations*

#### 12.3.1.1 Metal–Semiconductor Composites

There are numerous methods that are involved with the metal precursors' reduction and further deposit metal NPs on the semiconductors' surface, leading to the formation of metal–semiconductor composite. The common methods include photo-deposition method, alcohol reduction method, chemical reduction method (common reducing agents such as $NaBH_4$, ascorbic acid, glucose, trisodium citrate, hydrazine, etc.), deposition–precipitation (DP) method, atomic layer deposition (ALD) method, etc. (Table 12.1).

Xie et al. [10] synthesized Pt–$TiO_2$ composites with the use of three different methods: (1) photo-deposition of Pt NPs on titania with 300 W Xe lamp as light source and methanol as the sacrificial reagent, (2) impregnation of Pt precursor with titania and followed by calcination treatment in $H_2$ at 673 K, and (3) hydrazine reduction of $H_2PtCl_6$ an aqueous solution containing titania. The TEM results indicate that the photo-deposition method and hydrazine reduction method both result in smaller-sized Pt particles (mean size, 3.7 and 4.2 nm, respectively) and the impregnation method followed by $H_2$ calcination will result in bigger-sized Pt particles (6.8 nm). Wang et al. [9] adopted a unique tilted-target sputtering (TTS) method for the ultrafine Pt cluster deposition on 1D $TiO_2$ single-crystal film. The loading amount of Pt and cluster size (0.5–2 nm) were manipulated by adjusting the deposition time (5–60s). Song et al. [15] studied the shape-dependent Pd/$C_3N_4$ few-layer composites in CO2PR. During the synthesis process, the author used HCHO and $Na_2C_2O_4$ to promote the formation of Pd (111) facets, while the $Br^-$ and $I^-$ were introduced to stabilize the Pd (100) facet. As a result, Pd cube/$C_3N_4$ and Pd nanotetrahedron/$C_3N_4$ can be well obtained through a solution-phase solvothermal method. Despite their shape, these two Pd polyhedrons have comparable particle size (4–6 nm), which are the smallest Pd nanocrystals with specific facets obtained in aqueous phase by now.

Compared with single-unit metal–semiconductor composite, binary metal alloy NPs with diverse surface active sites and metal-support interfaces thus could possess more potential in photocatalysis. In the synthesis of alloy NPs involved with at least two metal precursors, Long et al. [18] synthesized a series of PdxCu1 fcc-phased NPs in situ growth on the $TiO_2$ nanosheet in the presence of ascorbic acid and PVP. Through varying the ratio of $K_2PdCl_4$ to $CuCl_2$, sphere-like NPs of CuPd1Cu1, Pd3Cu1, Pd5Cu1, Pd7Cu1, and Pd11Cu1 could be obtained. Neațu et al. [14]

adopted the stepwise deposition–precipitation method to prepare Au–Cu alloy/$TiO_2$ photocatalyst, using 0.2 M NaOH to tune the pH value of $TiO_2$-$HAuCl_4$ and Au/$TiO_2$-$Cu(NO_3)_2$ aqueous slurry to 8.5 and annealing in air and $H_2$ atmosphere, respectively. The Au–Cu alloy NPs were characterized by HR-TEM which constitute Au–Cu lattice fringes; meanwhile, the redshift of Au SPR adsorption peak in UV-vis DRS spectra also suggests the Au and Cu formed alloy status. It should be noted that, using this synthesis method, the unalloyed Au and Cu NPs also could be detected.

#### 12.3.1.2 Semiconductor Heterojunctions and Z-Scheme Composites

In order to develop the economic noble metal-free photocatalysts with high efficiency in CO2PR, some semiconductor junction composites have been developed; the common methods include hydrothermal/solvothermal method, impregnation method, self-template method, ALD method, etc. (Table 12.1).

Jin et al. [38] reported a hierarchical-structured Z-scheme CdS-$WO_3$ photocatalyst and applied it in CO2PR. The hierarchical hollow $WO_3$ spheres were formed by immersing $SrWO_4$ in $HNO_3$ at first, and then the precipitate was washed and calcined at 500 °C in air. The as-prepared $WO_3$ spheres were negatively charged at pH = 7; therefore, stepwise adding $Cd^{2+}$ and $S^-$ source slowly will generate heterostructure CdS–$WO_3$ composite. Wang et al. [34] developed a porous ZnO@$Co_3O_4$ composite by using ZIF-8 and ZIF-67 as precursor templates (Fig. 12.2). First, the ZIF-8@ZIF-67 core–shell structure was synthesized through a solvothermal process and then followed by a $N_2$-400 °C 2-h calcination and air-400 °C 2 h calcination treatment. The two-step calcination process was determined by the TG/DTA analysis, while one-step calcination under air atmosphere will lead to nonporous ZnO NPs.

In et al. [37] designed a novel CuO–$TiO_{2-x}N_x$ hybrid hollow nanocubes with the use of $CuN_3$ nanocubes as reactive templates (Fig. 12.3a). After slow hydrolysis of titanium-n-butoxide on the surface of $CuN_3$, the calcination treatment at 450 °C was carried out. During the calcination process, the $CuN_3$ reacts with the oxygen and form hollow CuO nanocube; meanwhile, the nitrogen diffuses outward and reacts with the crystalline $TiO_2$ to form $TiO_{2-x}N_x$. Park and coworkers [57] once proposed a novel $Cu_xO$–$TiO_2$ p–n heterojunction (Fig. 12.3b). The Cu/$Cu_2O$ nanoparticles were first synthesized through a thermal decomposition method, and then the $TiCl_4$ was mixed with the Cu/$Cu_2O$ NPs in argon; after calcination in air, the $TiCl_4$ crystallized to $TiO_2$, and the Cu/$Cu_2O$ NPs were oxidized to $Cu_xO$ with organic ligands removed at the same time; at last, the mesoporous $Cu_xO$–$TiO_2$ composites were obtained.

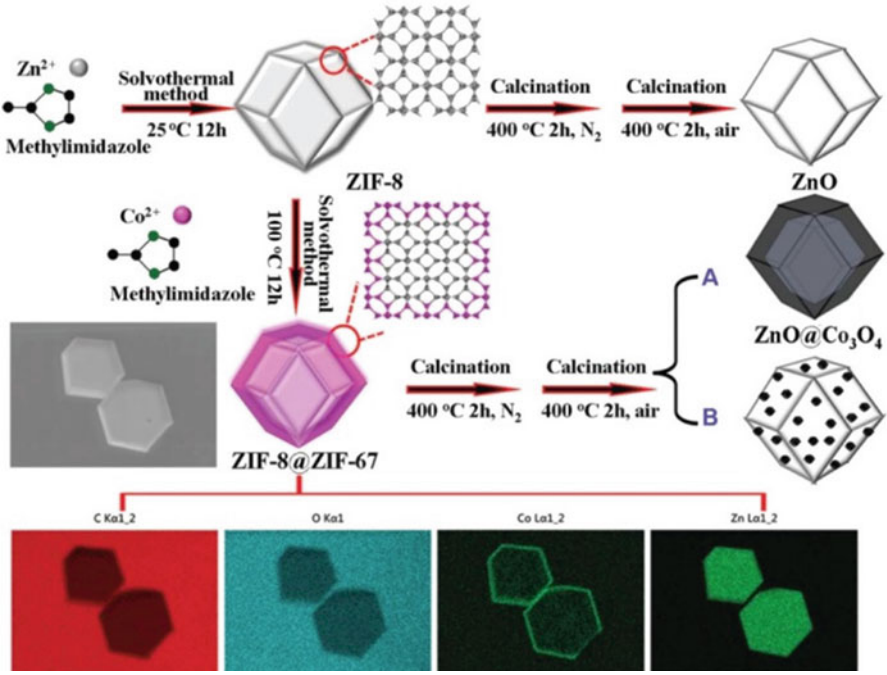


**Fig. 12.2** Schematic illustration of the synthesis of polyhedral ZnO and ZnO@$Co_3O_4$ originated from ZIF8 and ZIF-8@ZIF-67, respectively. (Reprinted with permission from Ref. [34]. Copyright 2016, Royal Society of Chemistry)

#### 12.3.1.3 Dual Cocatalysts

Considering the precise construct of the configuration of photocatalyst with synergistic dual cocatalysts will enhance the CO2PR efficiency greatly. Recently, more and more researches have focused on the dual cocatalysts deposition with advanced structures. Generally, compared with sole cocatalyst composites, the synthesis of dual cocatalysts is more complicated, which need involve with stepwise deposition of dual units. The spatial locations of dual cocatalysts should depend on the functions of these two species which are either separated or combined with each other.

The construction of spatial separated electron trapping agents and hole collectors could greatly promote the charge separation efficiency of the photocatalyst. Dong et al. [8] developed a 3D hierarchical structured $TiO_2$–$SiO_2$ with $CoO_x$ and Pt growing inside and outside of the skeleton. Firstly, the $Co(AC)_2.4H_2O$ and Ti–Si sol were mixed together and underwent a synchronizing self-assemble process; after the 500 °C calcination, the hydrolyzed $Co(OH)_x$ transformed into $CoO_x$ NPs embedded under the hierarchical $TiO_2$–$SiO_2$ skeleton homogenerously (denoted as the HCTSO). Subsequently, the Pt NPs were growing in situ on the outer surface of the HCTSO via alcohol reduction of $H_2PtCl_6$. In order to improve the $CO_2$

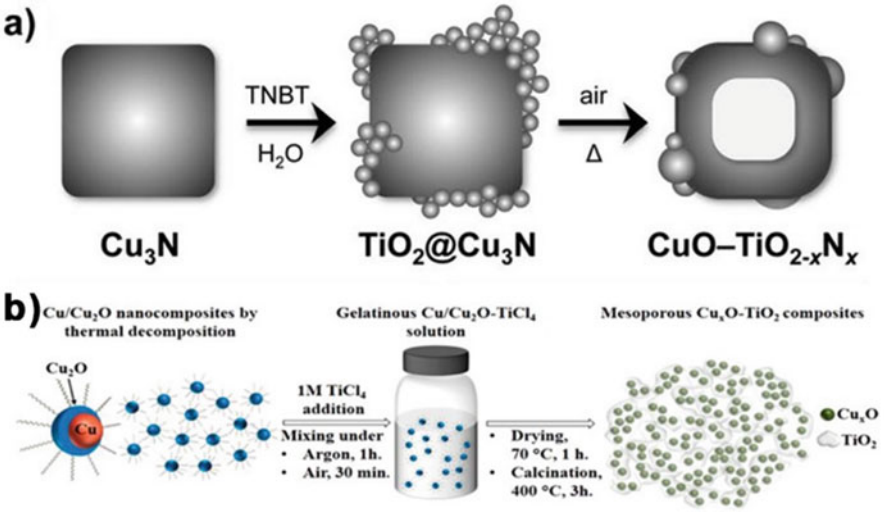


**Fig. 12.3** (**a**) Scheme illustration of multistep template strategy to convert $Cu_3N$ nanocube into $TiO_2@Cu_3N$ and hollow $CuO–TiO_{2-x}N_x$ nanocubes. Reprinted with permission from Ref. [37]. Copyright 2012 Jonh Wiley & Sons, Inc. (**b**) Scheme diagram of the step-by-step synthesis of mesoporous $Cu_xO–TiO_2$ composite. (Reprinted with permission from Ref. [57]. Copyright 2016, American Chemical Society)

adsorption and the selectivity toward $CH_4$, Pan et al. [47] developed a 5-nm-thick carbon layer coated on $In_2O_3$ nanobelt coupled with Pt NP+ loadings. The glucose was used as the carbon source and the carbon layer was formed at 600 °C under the Ar atmosphere. Afterward, the Pt NPs were deposited on the surface of carbon layer through a photo-deposition method. The loading amount of carbon layer and Pt are 8% and 2%, respectively. Another classic dual cocatalysts structure of $Pt@Cu_xO$ loaded on $TiO_2$ (p25) was proposed by Zhai and coworkers [41]. At first, $Pt–TiO_2$ was first prepared by photoreduction of $H_2PtCl_6$ in the $TiO_2$ suspension; afterward, the Cu species were deposited on the Pt surface under the illumination and using the $CuSO_4$ as the precursor. The Cu is easily oxidized into $Cu^1$ in air; therefore, the Cu existed as $Cu_xO$ form. Moreover, prolonging the photo-deposition time of Cu species will increase the $Cu_xO$ coverage on Pt NPs; the 5-h irradiation will form a complete $Pt@Cu_xO$ core–shell structure.

The all-solid-state Z-scheme photocatalysts could take advantage of more negative reduction potential electrons and more positive oxidation potential holes from different semiconductors counterparts, thus attract more and more attention in CO2PR. Generally speaking, the photosystem II (oxidation part PSII) and photosystem I (reduction part PSI) are connected by a conductor. Li et al. [45] developed an elegant all-solid Z-scheme $WO_3/Au/In_2S_3$ nanowire photocatalyst; the $WO_3$ nanowire was first grown on the tungsten foil under Ar flow with $WO_3$ powder as precursor, then Au NPs were deposited on $WO_3$ nanowire by plasma sputtering method, and the $In_2S_3$ shell coated on Au surface was finally obtained through a

chemical vapor deposition method ($In_2S_3$ powder and Au/$WO_3$ were placed in quartz furnace separately, the temperature of the furnace will be increased to 800 °C with certain Ar flow, and the deposition time is 10 min).

#### 12.3.1.4 Carbon-Based Cocatalysts

Besides the metal nanoparticles and semiconductors cocatalysts, there are intensive research works focusing on the carbon-based cocatalysts in CO2PR. Graphene, carbon nanotube, carbon nanodots, carbon nanosheet layer, metal organic frameworks (MOFs), metal–ligand complex, etc. are common carbon-based cocatalysts in recent years (Table 12.1).

Graphene, owing to its flexible mechanical strength, remarkable electric conductivity, high surface area, etc., has been applied to many fields. In photocatalysis, graphene can transfer the photo-generated electrons, hence improving the electron-hole separation efficiency and prolonging the lifetime of charge carriers (Fig. 12.5). Tu et al. [49] fabricated a sandwich structure $TiO_2$–graphene nanosheet over a one-step hydrothermal method. The graphene oxide (GO) was prepared according to Hummers' method which is a common method for many reported graphene–semiconductor composites. During the hydrothermal process, the GO, Ti precursor, and solvent (ethylenediamine abbreviated as En/$H_2O$) underwent an in situ simultaneous reduction–hydrolysis process, the GO was reduced by En, and the Ti precursor hydrolyzed to form $TiO_2$ NPs. Different weight ratios of $TiO_2$/graphene were obtained by varying the GO amount during the synthesis. Ong et al. [58] adopted the electrostatistic self-assembly strategy to prepare the reduced graphene oxide (rGO)/protonated $C_3N_4$ (pCN) composites. Owing to abundant CN motifs existing on the g-$C_3N_4$ surface, the surface protonation by HCl could be easily conducted. After the HCl treatment, the pCN was positively charged according to the Zeta potential test, which could spontaneously assemble on the negative-charged GO (prepared by Hummers' method). Finally, the GO was reduced to rGO by $NaBH_4$ to form 2D/2D rGO/pCN composite. Unlike 2D graphene–semiconductor composites, Zhang proposed that encapsulation by graphene-like carbon sheet could enhance the confinement effect of the core nanoparticles compared with its naked counterparts. Therefore, Fe@C NPs were fabricated for the use of MIL-101 as self-sacrificing template and precursor. During the synthesis, two-step calcination method was utilized; first, MIL-101(Fe) was collapsed and formed $Fe_3C$ and $Fe_3O_4$ in Ar-500 °C; meanwhile, the Fe species could avoid sintering into large NPs and , subsequently, the temperature raised to 700 °C to obtain the Fe@C NPs. It should be noted that rational regulate the calcination temperature and retention time is the key to control the particle size and graphite carbon layer's thickness.

Metal organic frameworks (MOFs), as one class of porous nanocrystals, possess huge surface area, tunable surface functional groups, and alternative compositions which have been applied to multiple fields such as catalysis, gas capture and separation, drug delivery, molecule identification, etc. Due to strong $CO_2$ adsorption capability of UiO-66, cooperation with some narrow bandgap semiconductor could

improve the CO2PR efficiency. Shi et al. [56] developed an electrostatic self-assembly strategy to fabricate the UiO-66/$C_3N_4$ composite. Firstly, the $C_3N_4$ nanosheet (CNNS) was prepared by liquid-state ultrasound exfoliation method; after the centrifuge to remove the large bulk $C_3N_4$, the CNNS was obtained. Secondly, the as-prepared UiO-66 and CNNS were mixed in water, because the CNNS is negatively charged in water with −35.91 mV Zeta potential and + 7.71 mV for UiO-66; that is the reason why electronic statistic self-assembly happened. Li et al. [53] developed a $Cu_3(BTC)_2$ (HKUST-1)@$TiO_2$ core–shell structured composite; the solid Cu precursor and the involvement of PVP are key to coat $TiO_2$ on the $Cu_3(BTC)_2$ nanocrystals uniformly. During the control experiments, using Cu $(OH)_2$ as Cu precursor and in the absence of PVP, the $TiO_2$ cannot be coated on the $Cu_3(BTC)_2$ uniformly; besides, using unsolid $Cu(NO_3)_2$ as precursor, the thermal stability of $Cu_3(BTC)_2$ is low; in this case, it will decompose at the 180 °C coating process and also cannot get desirable result.

Carbon nanodots, including carbon quantum dots, carbon dots, and graphene quantum dots, which are a new class of zero-dimensional (0D) carbon materials have attracted people's attention over the past few decades; the unique properties of carbon dots such as superior up-conversion and size-dependent photoluminescence, high stability, low cytotoxicity, earth abundance, etc., thus made it a plausible candidate in many fields. The synthesis of carbon nanodots can be roughly classified into two approaches: bottom-up approach and top-down approach. Kang et al. [59] reported a facile electrochemical approach to synthesize large-scale high-quality carbon dots. The authors used two graphite rods as the counter electrode and ultrapure water as the electrolyte; statistic potential with 15–60 V was applied to the two electrodes; after 120-h electrolysis, a dark-yellow solution was formed, and the water-soluble carbon dots were obtained after filter and centrifuge. Ong et al. [55] adopted glucose as the carbon source using alkali-assisted ultrasonication method to prepare carbon nanodots (CND). Briefly, glucose and NaOH solution was mixed together and sonicated for 2 h and resulted in a dark-brown solution; after neutralization and filter, a brown carbon dot solution was obtained. Owing to the natural properties of same negative polarity of $C_3N_4$ and carbon dots, the coupled CND/$C_3N_4$ in this paper was obtained by protonation $C_3N_4$ in HCl solution in advance; after that, the $C_3N_4$ is positively charged thus can attract the CND by electrostatic force.

## 12.4 Roles and Properties of Different Cocatalysts

### *12.4.1 Promote the Charge Separation and Transfer*

It is well-known that the noble metal NPs such as Pt, Pd, Au, Ag, Ru, etc. loaded onto the semiconductors could trap the photo-generated electrons and promote the separation of charge carriers. The reason could be attributed to the Fermi level of metal NPs which lies energetically below the conduction band level of its

semiconductor counterpart; besides, the Schottky barrier formed at the metal–semiconductor interface thus could prevent the electrons from flowing backward. In this way, the surface sites of metal NPs become the active sites for the CO2PR reduction, and the performance of the metal–semiconductor composite is highly depending on the electron trapping ability of the supported metal NPs.

Xie et al. [10] compared the activity of five noble metals (Ag, Au, Rh, Pt, Pd) supported on $TiO_2$ in CO2PR. The yield of $CH_4$ and the rate of total electrons' consumption in the CO2PR increase with the order of $TiO_2$ < Ag-$TiO_2$ < Rh-$TiO_2$ < Au-$TiO_2$ < Pd-$TiO_2$ < Pt–$TiO_2$, which equals with the same trend of the work function of these noble metals. This result reflects the fact that the electron trapping ability contributes to the reductive performance of supported metal catalyst and Pt–$TiO_2$ in this evaluation system is superior to the others. Since Pt is a very efficient cocatalyst in photocatalysis, the rational designation of Pt NPs with suitable shape (expose certain facets) and particle size (both geometric and electronic) is important. As we mentioned before, Wang et al. [9] synthesized a series of different-sized Pt NPs ranging from 0.5 to 1.5 nm loaded on the 1D $TiO_2$ single crystals through a TTS method, and the 1 nm Pt NPs show the highest $CH_4$ yield. The author claims that the ultrasmall Pt NPs (less than 1 nm) could prevent the electrons transferring from $TiO_2$ because of its higher energy band compared with the CB of $TiO_2$; on the contrary, bigger Pt NPs act as electron-hole recombination center which is also detrimental in the photocatalysis. Furthermore, the author adopted the femtosecond time-resolved TA spectroscopy to elucidate the charge transfer dynamics. After liner fitting, Pt–$TiO_2$ shows a greater slope compared with its $TiO_2$ counterpart which directly reflects the Pt NPs suppress the charge recombination process.

In order to replace the expensive noble metal cocatalysts into some earth-abundant materials, the development of noble metal-free cocatalysts with comparable performance is essential. Among them, carbon dots and graphene also play key role in promoting the charge separation in photocatalysis. Ong et al. [55] report carbon nanodots (CND) supported on protonated $C_3N_4$ composite. The obtained CND/pCN shows the CND with 4.4 nm diameter dispersed well on the pCN surface, and the CND did not affect the adsorption edge of $C_3N_4$ but act as conductive electron channel for charge separation (Fig. 12.4a, b). The author adopted steady-state PL spectroscopy and time-resolved transient PL decay to verify the charge separation kinetics. The pure p-$C_3N_4$ shows an intensive and broad PL emission peak which means a great extent of electron-hole recombination; the CND/pCN hybrids on the other hand show obvious decrease of peak intensity which suggests the recombination of charge carriers were suppressed (Fig. 12.4c). The emission lifetime of CND/pCN reduced compared with pCN which means the rapid interfacial electrons inject from pCN to CNDs and participate in the CO2PR reaction (Fig. 12.4d). Besides the electrons' trapping ability, CNDs also can serve as the photosensitizer. Yu et al. [60] reported CDs/$TiO_2$ composite with enhanced visible light hydrogen production rate. The author claimed that π-conjugated CDs sensitize $TiO_2$ by forming C-O-Ti bond and donate electrons under visible light irradiation.

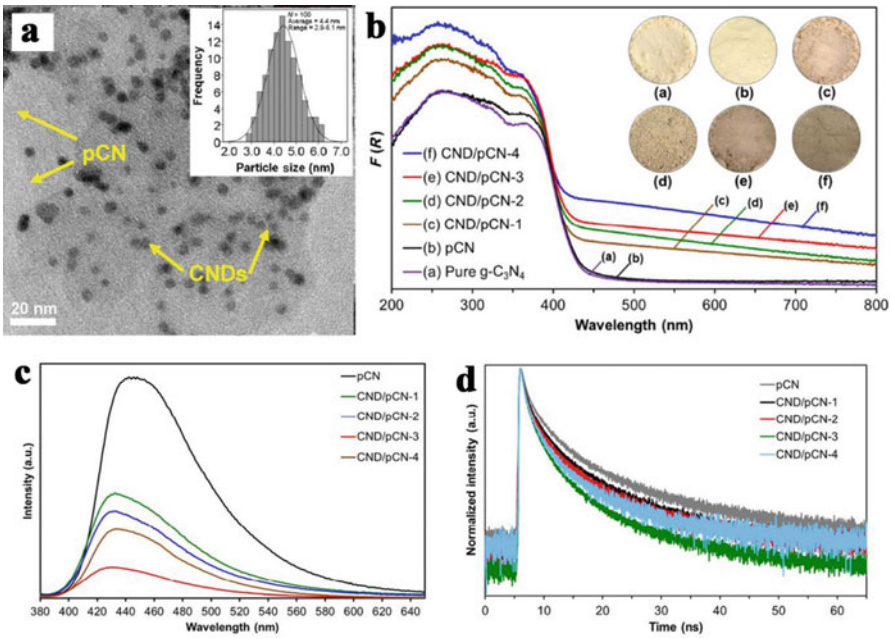


**Fig. 12.4** (**a**) TEM image of CND/pCN-3 sample, the inset image shows the particle size distribution of CNDs deposited on the pCN nanosheet. (**b**) UV–vis DRS spectra of different samples; the digital photographs showing the colors of different samples are inset. (**c**) PL spectra of pCN and CND/pCN samples. (**d**) Time-resolved transient PL decay curves of pCN and CND/pCN samples excited at 405 nm. (Reprinted from Ref. [55]. Copyright 2017, Wee-Jun Ong et al. licensee Springer)

When graphene was introduced as the cocatalyst, Yu et al. [54] developed a metal-free CdS/rGO composite with enhanced $CH_4$ generation rate (2.51 μmol/g·h) which is ten times higher than pure CdS rods and overperforms the Pt/CdS. The enhanced performance was attributed to the π–π conjugate interaction between $CO_2$ and graphene and thus improves the $CO_2$ adsorption amount and destabilizes $CO_2$; besides, the rGO promotes the electron transfer, and storage was confirmed by conducting transient photocurrent and impedance analysis (Fig. 12.5b). Recently, Xu et al. [52] reported a $CsPbBr_3$ perovskite graphene composite which could efficiently convert $CO_2$ into $CH_4$ with 99.3% selectivity. The author also adopted steady-state PL and time-resolved PL decay to probe the electron transfer dynamic. Distinct PL intensity quenching of $CsPbBr_3$ QD and the PL decay time of $CsPbBr_3$ QD/GO composite are shorter compared with $CsPbBr_3$ QDs, which both reflect the introduction of GO benefits to the electron transfer and suppress the electron-hole recombination (Fig. 12.5d).

Construction of the semiconductors' heterojunction is another strategy to improving the charge separation efficiency in CO2PR. Shi et al. [61] reported a visible light responsive g-$C_3N_4$/$NaNbO_3$ nanowire with higher CO2PR activity than either g-$C_3N_4$ or $NaNbO_3$. From Fig. 12.6 (a), the HR-TEM image shows the obvious

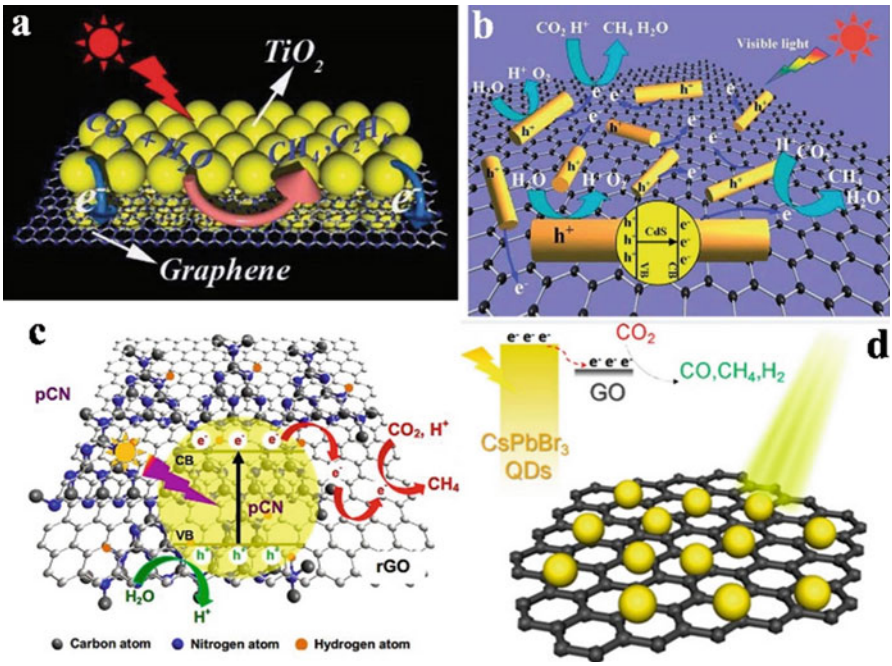


**Fig. 12.5** (**a**) Schematic illustration of charge separation and transfer in G-$TiO_2$ system and photoreduction of $CO_2$ and $H_2O$. Reprinted with permission from Ref. [49]. Copyright 2013 Jonh Wiley & Sons, Inc. (**b**) Schematic illustration of charge separation and transfer in CdS-rGO composite. Reprinted with permission from Ref. [54]. Copyright 2014 Royal Society of Chemistry. (**c**) Schematic illustration of the charge transfer and separation in rGO/pCN nanocomposite for $CO_2$ photoreduction with $H_2O$ to $CH_4$. Reproduced from Ref. [58] with permission of Elsevier. (**d**) Schematic diagram of $CO_2$ photoreduction over $CsPbBr_3$ QDs/rGO. (Reprinted with permission from Ref. [52]. Copyright 2017 American Chemical Society)

intimate interface, which implies the existence of heterojunction between $C_3N_4$ and $NaNbO_3$. The band structures of g-$C_3N_4$ and $NaNbO_3$ were determined by UV–vis DRS and VB-XPS in Fig. 12.6 (b, c). The wavelength (λ) of adsorption edge of g-$C_3N_4$ and $NaNbO_3$ is 365 nm and 450 nm, respectively; therefore, the $E_g$ (bandgap energy = 1240/λ) was calculated to be 3.4 eV and 2.7 eV, respectively. Meanwhile, the VB XPS result shows that the $E_{VB}$ (valence band energy) of g-$C_3N_4$ and $NaNbO_3$ was located at ~1.57 eV and 2.7 eV, respectively; therefore, the $E_{CB}$ (conduction band energy) of g-$C_3N_4$ and $NaNbO_3$ was calculated to be −1.13 eV and − 0.77 eV based on the equation $E_{CB} = E_{VB} - E_g$. Since the CB level of $C_3N_4$ is more negative than $NaNbO_3$, the photo-excited electrons from $C_3N_4$ could migrate to $NaNbO_3$ and suppress the electron-hole carriers' recombination.

Although p–n heterojunctions greatly inhibit the recombination of photo-generated electrons and holes, however, after the photo-generated electrons migrate to the CB with lower reduction potential, the redox ability of the integral composite

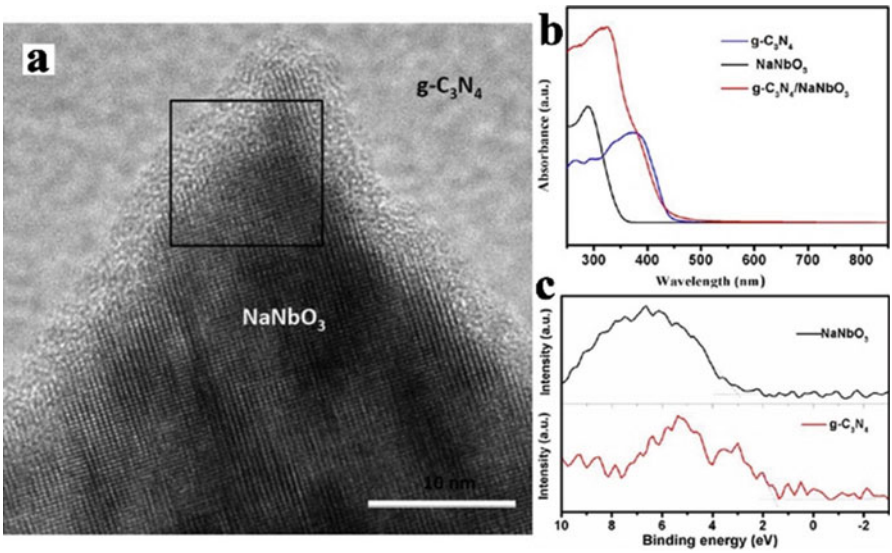


**Fig. 12.6** (**a**) HR-TEM image of g-$C_3N_4$/$NaNbO_3$ heterojunction. (**b**) UV–vis DRS spectra of different samples. (**c**) VB-XPS spectra of g-$C_3N_4$ and $NaNbO_3$. (Reprinted with permission from Ref. [61]. Copyright 2014, American Chemical Society)

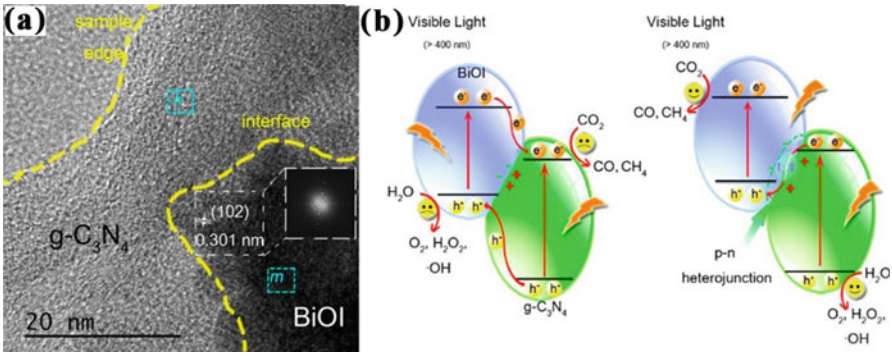


**Fig. 12.7** (**a**) HR-TEM image of 7.4-BiOI/$C_3N_4$ composite. (**b**) Schematic illustrations of double-charge transfer mechanism (left) and Z-scheme charge transfer mechanism (right). (Reprinted with permission from Ref. [39]. Copyright 2016 American Chemical Society)

will be impaired [23]. Therefore, the all-solid-state Z-scheme system was developed to solve this problem. Generally, the all-solid-state Z-scheme photocatalytic system (PS) was divided into two components: PS-PS and three-component PS-conductor (C)-PS. Wang et al. [39] construct an indirect PS-PS Z-scheme BiOI/$C_3N_4$ composite with enhanced visible light CO2PR performance (Fig. 12.7a). In order to investigate the charge transfer modes, the author proposed two possible charge transfer routes: double-transfer mechanism and Z-scheme mechanism. The contrast

experiment was adopted by using visible light as the light source; the result of no product yield proved that the electron transfer was not followed by the previous one. Furthermore, when the EDTA was added as the hole scavengers, the result shows an improved CO and $H_2$ yield but decreased $O_2$ yield which further reflects the enhanced electron-hole separation (Fig. 12.7b).

Compared with the PS–PS Z-scheme, the interface between two solids usually contains many defects, which may inhibit the charge transfer. Therefore, the PS-C-PS Z-scheme with a conductor insertion could reduce the electron transfer resistance and thus improve the CO2PR efficiency. He et al. [25] reported an $Ag_3PO_4/C_3N_4$ composite with enhanced CO2PR activity. Since the $Ag_3PO_4$ is not stable, therefore, Ag NPs were formed in situ within the composites under light irradiation and acted as the electron mediator. Taking into account of the CB level of $Ag_3PO_4$ (0.45 eV), if the composites followed the double-charge transfer mechanism, the introduction of $Ag_3PO_4$ cannot promote the CO2PR. So it is reasonable to believe that the charge transfer route followed Z-scheme mechanism. In this way, Ag accepts the photo-generated electrons from $Ag_3PO_4$ and recombines with holes from $C_3N_4$; subsequently, the photo-generated electrons with more negative reduction potential could be used into the CO2PR reaction. Wei et al. [44] developed a PS–C–PS Z-scheme structure photocatalyst that contains CdS (shell), Pt (core), and $TiO_2$ (support), which show enhanced $CO_2$ photoreduction activity and selectivity (36.8 μmol/g.h $CH_4$ yield and 98.1% $CH_4$ selectivity). The location of reduction sites and electron transfer route was confirmed by Ag photo-deposition method. The Ag NPs selectively deposited on the shell of CdS instead of $TiO_2$ surface which clearly demonstrates that the CdS acts as the reduction site and the electron transfer follows the $TiO_2 \rightarrow Pt \rightarrow CdS$ route. In order to present consolidate proof to Z-scheme charge transfer behavior, Li et al. [45] first adopt Kelvin probe force microscopy to detect surface potential change of $In_2S_3$-Au-$WO_3$. Compared with $WO_3/In_2S_3$, the SPV image (reflect the concentration of photo-generated holes) of $WO_3/Au/In_2S_3$ shows significant change from 10 mV to 30 mV; this difference vividly reflects the efficient charge separation and the role of Au as the electron mediator.

Another way to improve the charge separation efficiency in photocatalysis is the construction of double cocatalysts (usually refers to the electron trapping agent and hole collect agent) with spatial separated configurations. Domen and coworkers [62] first developed $Ta_3N_5$ photocatalyst hollow shell with Pt and $CoO_x$ deposited inside and outside of the shell, respectively. Followed by this pioneered work, similar strategies have been proposed such as the thin heterojunction Pt–$TiO_2$@$In_2O_3$@$MnO_x$ hollow shell structure, porous $TiO_2$ tube, or hollow $C_3N_4$ shell with spatial separated Pt and $CoO_x$ NPs [63–65], etc. Recently, our group developed a new strategy to construct spatial configuration by introducing Pt NPs and $CoO_x$ NPs outside and inside of the skeleton of hierarchical $TiO_2$-$SiO_2$ (HTSO) [8], abbreviated as Pt/HCTSO. The HR-TEM image clearly indicates that the Pt NPs and $CoO_x$ NPs separated by the HTSO skeleton (Fig. 12.8a); on the other hand, EDS-mapping image shows the Pt and Co species are well-dispersed throughout the framework of HTSO and no aggregation happened (Fig. 12.8b). The $CO_2$ photoreduction evaluation result revealed that the 0.8% Pt/HCTSO (0.8%) shows enhanced

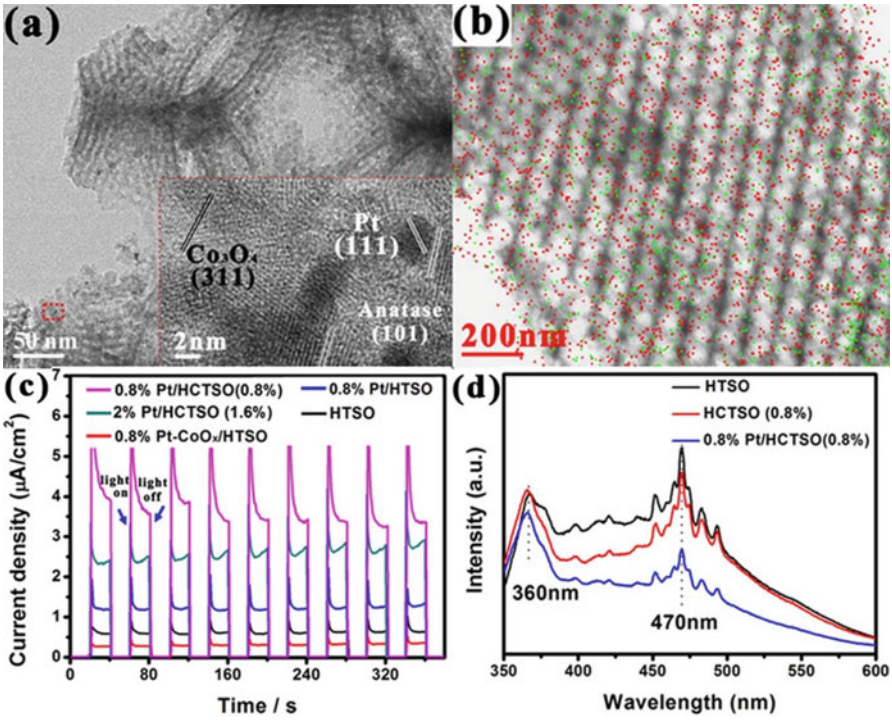


**Fig. 12.8** (**a**) TEM and selective HR-TEM images of Pt/HRTSO. (**b**) Elemental mapping image of Pt/HRTSO, the red dots denote as Pt element and the green dots denote as Co element. (**c**) Transient photocurrent spectra of different samples (300 W Xe lamp with AM 1.5 filter was used as the light source and 0.5 M $Na_2SO_4$ solution is used as the electrolyte). (**d**) Room temperature PL spectra of different samples (excitation wavelength at 315 nm). (Reprinted with permission from Ref. [8]. Copyright 2016, Royal Society of Chemistry)

$CH_4$ yield and selectivity for $CH_4$ which are 1.9 and 4.4 times higher than 0.8% Pt/HTSO. To highlight the spatial locations of Pt and $CoO_x$ in CO2PR, the Pt-$CoO_x$/HTSO was prepared by randomly loading Pt and $CoO_x$ on the surface of HTSO; the CO2PR result shows even lower $CO_2$ reduction activity. The enhanced transient photocurrent response and decreased intensity of PL emission peaks (360 and 470 nm) all confirmed the spatial separated double cocatalysts promote the charge separation effectively (Fig. 12.8c, d). On the contrary, the random loading of Pt and $CoO_x$ on the surface of HTSO results in many electron-hole recombination centers, which is detrimental to charge separation and thus shows poor performance in CO2PR.

### 12.4.2 Improve $CO_2$ Adsorption and Activation

The $CO_2$ adsorption and activation on the surface of photocatalyst are two important steps; however, without modification, common semiconductor-based photocatalysts often show low $CO_2$ uptake. Therefore, combining some unique cocatalysts with higher $CO_2$ adsorption amount should be a proper way to improve CO2PR efficiency. Xie et al. [66] in the use of MgO, a basic metal oxide, as the cocatalyst deposited on the $TiO_2$ surface, with the addition of Pt NPs, the Pt-MgO/$TiO_2$ composite shows an enhanced activity for $CH_4$ production. During the experiments, a linear relationship between different $CO_2$ chemisorption by different basic metal oxide-modified Pt–$TiO_2$ and $CH_4$ yields clearly demonstrates the important role of $CO_2$ adsorption; the MgO modification shows the highest $CO_2$ chemisorption compared with other basic metal oxides. Besides, the optimal MgO content is measured to be 1%; excess MgO adding will cause a thicker MgO layer and cover the Pt sites which are detrimental for $CO_2$ photoreduction. Li et al. [53] adopt MOF ($Cu_3(BTC)_2$) as the $CO_2$ adsorption cocatalyst and coat porous $TiO_2$ shell on the MOF crystals' surface. This unique design hybrid shows enhanced $CH_4$ yield and selectivity compared with bare $TiO_2$ counterpart. The $CO_2$ adsorption results between bare MOF and MOF@$TiO_2$ suggest the $CO_2$ molecules can easily pass the $TiO_2$ shell. In order to investigate the charge transfer and working mechanism, the author adopts TA analysis and first-principle simulation. The result indicates the photo-excited electrons can transfer to the MOF core; subsequently, the $CO_2$ molecules adsorbed in MOF can be activated and convert into $CH_4$ effectively. Similarly, Shi et al. [56] reported a $C_3N_4$/UiO-66 composite, in this work zirconium-based MOF: UiO-66 acts as both $CO_2$ absorber and a semiconductor-like material to promote the electron-hole separation. ESR was used to verify the electron transfer route. Specifically, signal of $g = 2.009$ is attribute to $O_2^-$ which was found in $C_3N_4$/UiO-66 under visible light irradiation but absent in pristine UiO-66. This indicates that the $C_3N_4$ was performed as a photosensitizer; the photo-generated electrons transferred to UiO-66 and thus suppress the electron-hole recombination and enhance the CO2PR performance. Pan et al. [47] reported a carbon-coated $In_2O_3$ photocatalyst with the use of glucose as the carbon source; the 5 nm carbon layer could enhance the $CO_2$ chemisorption and suppress the hydrogen generation (Fig. 12.9). Compared with the pure $In_2O_3$ nanobelt, C-$In_2O_3$ shows enhanced $CO_2$ adsorption capacity compared with pristine $In_2O_3$ nanobelt, and the maximum $CO_2$ adsorption was reached with the use of 0.8 g glucose (Fig. 12.9b). The selectivity of $CH_4$ was studied by the thermodynamic and kinetic behavior of H proton transfer route in the assistance of DFT calculation. The result indicates that the H proton transfer to adsorbed $CO_2$ in $Pt_2$/C-$In_2O_3$ is easier than $H_2$ formation (endothermic); on the contrary, H proton reduction to $H_2$ on $Pt_2$/P-$In_2O_3$ is exothermic, which is easier than $Pt_2$/C-$In_2O_3$. This result well-explained the high $CH_4$ yield and CO2PR selectivity of Pt/C-$In_2O_3$ compared with Pt/P-$In_2O_3$.

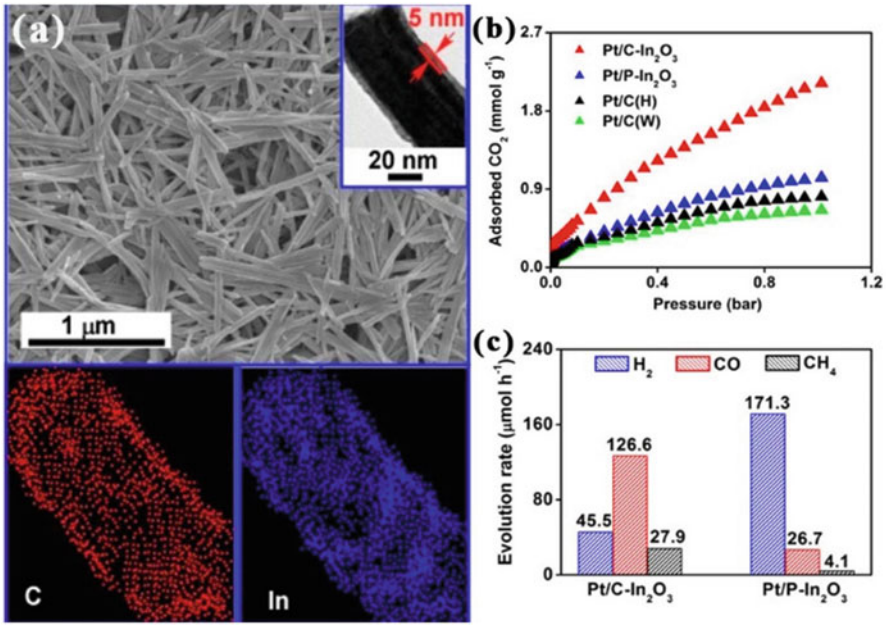


**Fig. 12.9** (**a**) SEM and TEM (inset) images and EDX elemental mapping images of C-$In_2O_3$. (**b**) $CO_2$ adsorption capacities of $In_2O_3$-based samples. (**c**) $H_2$, CO, and $CH_4$ evolution rates from $CO_2$ photoreduction on Pt/C-$In_2O_3$ and Pt/P-$In_2O_3$. (Reprinted with permission from Ref. [47]. Copyright 2017, American Chemical Society)

### *12.4.3 Surface Active Sites in $CO_2$ Photoreduction*

For better understanding the roles of cocatalysts in CO2PR, the identification of the active sites in cocatalysts and the study of reaction mechanism are very important. Only in this way can we develop photocatalysts with both high performance and selectivity in CO2PR. In order to investigate the active facet of Pd in $CO_2$ photoreduction, Bai et al. [15] synthesized Pd cube NPs (exposed mainly (100) facets) and Pd tetrahedron NPs (exposed mainly (111) facets) and deposit them on $C_3N_4$ layer separately. The size of Pd with different shapes is all around 4–6 nm; however, the activity was quite different, and the selectivity toward CO2PR of Pd nanotetrahedrons/$C_3N_4$ is obviously higher than Pd nanocubes/$C_3N_4$. Deep understanding of the shape-dependent selectivity of Pd was investigated by first-principle theory. Firstly, the adsorption energy for $CO_2$ and $H_2O$ on Pd (111) is 0.23 eV and 0.37 eV and for Pd (100) is 0.064 and 0.554 eV, which indicates the $CO_2$ and $H_2O$ tend to adsorb on Pd (111) and Pd (100), respectively. Secondly, when accepting two electrons, the Pd (111) shows a lower $CO_2$ activation energy barrier compared with Pd (100). This result reflects that the Pd (111) is the active site for $CO_2$ reduction and Pd (100) is more active for $H_2O$ reduction. Generally, the active sites of supported metal catalysts rely on two factors: surface geometric structure and electronic

structure, therefore, lattice engineering through alloy different metals could tuning the above two factors and further improve the activity and selectivity of the catalyst. $Pd_7Cu_1$ supported on $TiO_2$ nanoplates with isolation Cu in Pd lattice for CO2PR was reported by Long and coworkers [18]. In this research, when the Cu loading amount is below 12.5%, the XAFS results show that the oxidation of Cu (absent of Cu-O) could be inhibited effectively and Cu atoms were isolated in the Pd lattice (absent of Cu–Cu bonds). During the CO2PR evaluation, the $Pd_7Cu_1/TiO_2$ sample shows the optimal $CO_2$ reduction activity and $CH_4$ selectivity. In situ DRIFTS experiments show the enhanced signals of $HCO_3^-$, $CO_3^=$, and $CO_2^-$ species over samples with isolation of Cu atoms; in addition, the first-principle theory also indicate the Pd–Cu pairs could enhance the $CO_2$ adsorption. Both experimental and theoretical results suggest the Pd-Cu pairs favor the $CO_2$ adsorption. The different d band centers of Cu in $Pd_7Cu_1$ and $Pd_1Cu_1$ revealed the Pd-surrounded environment could tune the electronic structure of Cu and improve the catalytic activity of Cu. Au–Cu alloy NPs supported on $TiO_2$ (p25) reported previously also show enhanced performance in CO2PR compared with $Au/TiO_2$ or $Cu/TiO_2$ (Fig. 12.10) [14].

To gain deep understanding of the reaction mechanism and intermediates along the CO2PR, time-resolved in situ FTIR was applied. During the reaction, the generation of Cu-CO band (2126 $cm^{-1}$) indicates the Cu favors the $CO_2$ reduction instead of $H_2O$ reduction; also the $CO_2^{\cdot-}$ (1589 $cm^{-1}$) shows a continuously decreasing trend during the irradiation, which is assumed as a reactive species generated from the surface $Ti^{3+}$ (Fig. 12.10c, d). Further studies were carried out by using two light sources (visible light and UV light) to trigger CO2PR. Under the visible light irradiation, $CH_4$ and $H_2$ were the main products over the optimal $Au\text{-}Cu/TiO_2$, indicates the hot electrons generated from the surface plasma resonance of Au NPs and reacts with the activated $CO_2$ to generate $CH_4$. However, when using UV light as the light source, the Au–Cu alloy NPs act as the electron sink and promote the charge separation, which generate higher amount of $H_2$.

Low-coordinated sites (i.e., edge or corner sites) in metal NP-supported catalyst are often treated as active sites. Generally, these low-coordinated sites possess unique properties like strong binding energy toward certain reaction intermediates and low free energy which to some rate determines steps. Combining the experimental results with the DFT calculation, Mistry et al. [67] proposed that, in $CO_2$ electroreduction reaction, Au NPs show the size-dependent activity; the smaller-sized Au with more low-coordinated sites is more active in HER than CRR. Gao et al. [68] studied the Pd NPs with variable size in $CO_2$ electroreduction, and the result shows that low-coordinated sites of Pd are more suitable for COOH* generation but HER is insensitive to different surface sites. Zhu et al. [16] synthesized Pd nanosheet with similar thickness but different size ($TiO_2$-Pd NSs-s, small; $TiO_2$-Pd NSs-m, middle; $TiO_2$-Pd NSs-l, large) and proposed the edge sites of Pd nanosheet are the active site for CO2PR. Keeping the Pd loading amount as constant, with decrease of the size of Pd nanosheet, results in increased Pd edge density, and the CO and $CH_4$ yield increased as well. So the edge sites of Pd may act as the active site in CO2PR; to further confirm this edge-dependent activity, the Pd nanorings with even smaller size and higher density of edge sites were prepared and deposited on $TiO_2$

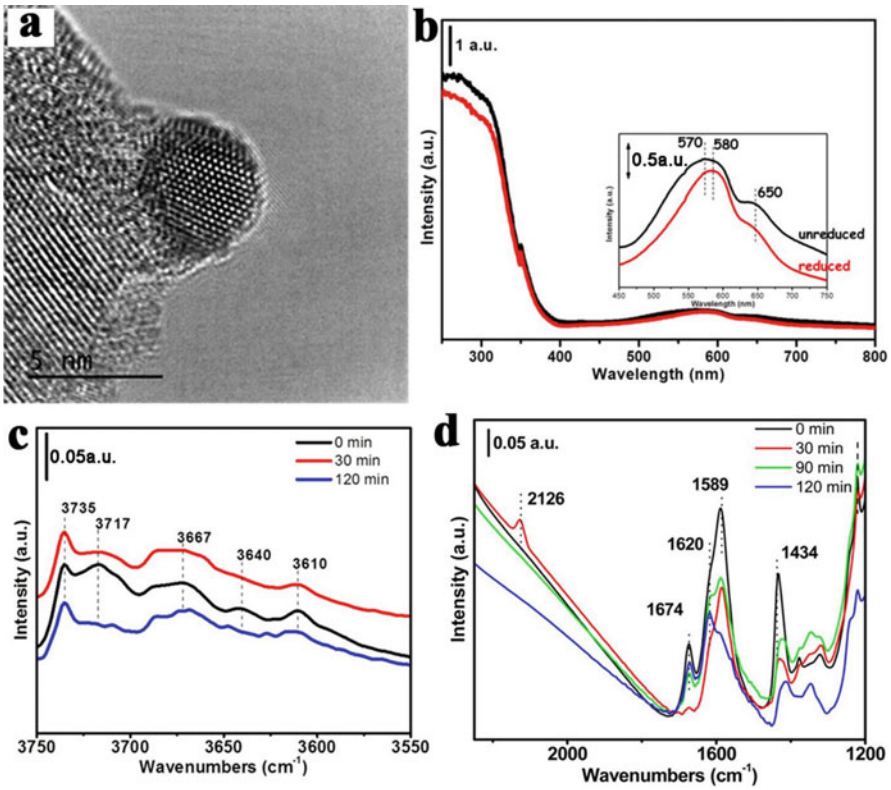


**Fig. 12.10** (**a**) HR-TEM image of Au–Cu alloy loaded on $TiO_2$; the lattice spacing distance is 0.222 nm, which is different from Au or Cu. (**b**) UV–vis DRS spectra of Au–Cu/$TiO_2$ (Au/Cu = 1:2) sample before and after reduction in 400 °C $H_2$ atmosphere calcination. (**c** and **d**) Time-resolved in situ FTIR spectra of intermediates that generate from adsorption and evolution during irradiation of $CO_2$ and $H_2O$ bounded on Au–Cu/$TiO_2$ (Au/Cu = 1:2). (Reprinted with permission from Ref. [14]. Copyright 2014, American Chemical Society)

(denoted as $TiO_2$-Pd NRs-s). The obtained $TiO_2$-Pd NRs-s show a lower $TiO_2$-Pd interface to Pd volume but higher edge to volume ratio compared with $TiO_2$-Pd NSs-s. Consequently, the $TiO_2$-Pd NRs-s show a higher CO2PR activity but lower HER yield (lower electron transfer ability). As a result, the density of edge sites of Pd is highly related with the CO2PR performance which is reasonable to assume as the active sites. To verify the roles of metal active sites in CO2PR more specifically, with the assistance of DFT calculation, Gao et al. [69] report a step-by-step $CO_2$ photoreduction over single-atom Pt or Pd supported on g-$C_3N_4$. The calculated relative binding energy between Pd and Pt within $C_3N_4$ sixfold cavity proved the existence of charge transfer and strong interaction between the metal and support. Two possible product pathways, HCOOH and CH3OH, are studied for Pd/$C_3N_4$. The calculated desorption energy barrier for the key intermediate HCOOH* on Pd/C3N4 is 0.46 eV, which is much lower than the formation of HCHO*, suggesting

that HCOOH is the more preferred product than $CH_3OH$. For $Pt/C_3N_4$, the strong interaction between Pt and HCOOH* (1.06 eV) and the favorable $CH_2$* and $H_2O$* generation instead of $CH_2OH$* hydrogenation made it the suitable candidate for $CH_4$ production.

## 12.5 Summary and Perspective

So far, the synthesis of photocatalyst with cocatalysts incorporation and the unique properties of various cocatalysts in CO2PR have been carefully summarized. The roles of these cocatalysts such as promote the charge separation efficiency, improve the adsorption of the $CO_2$ amount, expand the light harvesting range, provide active sites for the activation of $CO_2$ or other intermediates, etc. also have been briefly discussed. Besides, the important roles of spatial configurations of the photocatalyst composite and the deposition amount of the cocatalysts are also illustrated carefully: inappropriate incorporation of cocatalysts would lead to negative effect of the photocatalyst's performance; on the contrary, rational structure design such as the Z-scheme model or cocatalysts with spatial separated configurations could enhance the performance of the photocatalyst. It should be noted that we mainly focus on the solid-state cocatalysts in this chapter; beside this, the molecular-state cocatalysts like metal complex and dyes also could act as the cocatalyst in the CO2PR; however, this type of photocatalytic system is often conducted in the liquid phase and in the presence of hole scavenger, which is quite different from the solid-phase cocatalysts, so these types of cocatalysts are not discussed in here.

Although numerous efforts have been done in the selection of suitable cocatalysts and the development of fine structures of photocatalyst in CO2PR, many problems still existed and need to be answered and improved:

1. The CO2PR evaluation method is alternative among different research groups; therefore, the product yields comparison of different photocatalysts which is problematic; other evaluation methods such quantum yield efficiency and turnover number (TON) are highly encouraged in the following studies.
2. The origination of the products should be verified carefully; the organic impurities or carbon-involved species also could be converted into the products and cause the illusion result; therefore, control experiment of $CO_2$ photocatalytic reduction reaction should be conducted with the use of isotope-labeled $^{13}CO_2$ as the reactant for comparison.
3. The reaction pathways and mechanism in CO2PR are still ambiguous; deep understanding of the CO2PR could bring inspiration to the researchers to design highly efficient and selective catalysts; in this case, the DFT calculation along with the in situ characterizations is highly advocated.
4. The stability of the cocatalysts in the long-term CO2PR reaction is another concern; many photocatalysts suffer from low stability due to the carbon-involved species accumulation and deactivate gradually; therefore, the

development of highly efficient and stable photocatalyst and the study of the reason of catalysts' deactivation are important.

## References


1. Marszewski M, Cao S, Yu J, Jaroniec M (2015) Semiconductor-based photocatalytic $CO_2$ conversion. Mater Horiz 2(3):261–278
2. Walsh B, Ciais P, Janssens IA, JP ˜u, Riahi K, Rydzak F, DPv V, Obersteiner M (2017) Pathways for balancing $CO_2$ emissions and sinks. Nat Commun 8:14856–14868
3. Fujishima A, Honda K (1972) Electrochemical photolysis of water at a semiconductor electrode. Nature 238:37–38
4. Ma Y, Wang X, Jia Y, Chen X, Han H, Li C (2014) Titanium dioxide-based nanomaterials for photocatalytic fuel generations. Chem Rev 114(19):9987–10043
5. Habisreutinger SN, Schmidt-Mende L, Stolarczyk JK (2013) Photocatalytic reduction of $CO_2$ on $TiO_2$ and other semiconductors. Angew Chem Int Ed 52(29):7372–7408
6. Dong C, Xing M, Zhang J (2016) Economic hydrophobicity triggering of $CO_2$ photoreduction for selective $CH_4$ generation on noble-metal-free $TiO_2$-$SiO_2$. J Phys Chem Lett 7:2962–2966
7. Li K, Peng B, Peng T (2016) Recent advances in heterogeneous photocatalytic $CO_2$ conversion to solar fuels. ACS Catal 6:7485–7527
8. Dong C, Xing M, Zhang J (2016) Double-cocatalysts promote charge separation efficiency in $CO_2$ photoreduction: spatial location matters. Mater Horiz 3(6):608–612
9. Wang W, An WJ, Ramalingam B, Mukherjee S, Niedzwiedzki DM, Gangopadhyay S, Biswas P (2012) Size and structure matter: enhanced $CO_2$ photoreduction efficiency by size-resolved ultrafine Pt nanoparticles on $TiO_2$ single crystals. J Am Chem Soc 134(27):11276–11281
10. Xie S, Wang Y, Zhang Q, Deng W, Wang Y (2014) MgO- and Pt-promoted $TiO_2$ as an efficient photocatalyst for the preferential reduction of carbon dioxide in the presence of water. ACS Catal 4(10):3644–3653
11. Feng X, Sloppy JD, LaTempa TJ et al (2011) Synthesis and deposition of ultrafine Pt nanoparticles within high aspect ratio $TiO_2$ nanotube arrays: application to the photocatalytic reduction of carbon dioxide. J Mater Chem 21:13429–13433
12. Manzi A, Simon T, Sonnleitner C, Doblinger M, Wyrwich R, Stern O, Stolarczyk JK, Feldmann J (2015) Light-induced cation exchange for copper sulfide based $CO_2$ reduction. J Am Chem Soc 137(44):14007–14010
13. Mao J, Ye L, Li K et al (2014) Pt-loading reverses the photocatalytic activity order of anatase $TiO_2$ {001} and {010} facets for photoreduction of $CO_2$ to $CH_4$. Appl Catal B-Environ 144:855–862
14. Neatu S, Macia-Agullo JA, Concepcion P, Garcia H (2014) Gold-copper nanoalloys supported on $TiO_2$ as photocatalysts for $CO_2$ reduction by water. J Am Chem Soc 136(45):15969–15976
15. Bai S, Wang X, Hu C, Xie M, Jiang J, Xiong Y (2014) Two-dimensional g-$C_3N_4$: an ideal platform for examining facet selectivity of metal co-catalysts in photocatalysis. Chem Commun (Camb) 50(46):6094–6097
16. Zhu Y, Xu Z, Jiang W et al (2017) Engineering on the edge of Pd nanosheet cocatalysts for enhanced photocatalytic reduction of $CO_2$ to fuels. J Mater Chem A 5(6):2619–2628
17. Li N, Liu M, Yang B et al (2017) Enhanced photocatalytic performance toward $CO_2$ hydrogenation over nanosized $TiO_2$-loaded Pd under UV irradiation. J Phys Chem C 121(5):2923–2932
18. Long R, Li Y, Liu Y et al (2017) Isolation of Cu atoms in Pd lattice: forming highly selective sitesfor photocatalytic conversion of $CO_2$ to $CH_4$. J Am Chem Soc 139:4486–4492
19. Kong D, Tan JZY, Yang F, Zeng J, Zhang X (2013) Electrodeposited Ag nanoparticles on $TiO_2$ nanorods for enhanced UV visible light photoreduction $CO_2$ to $CH_4$. Appl Surf Sci 277:105–110

20. Kuriki R, Matsunaga H, Nakashima T, Wada K, Yamakata A, Ishitani O, Maeda K (2016) Nature-inspired, highly durable $CO_2$ reduction system consisting of a binuclear Ruthenium (II) complex and an organic semiconductor using visible light. J Am Chem Soc 138 (15):5159–5170
21. Li K, Peng T, Ying Z, Song S, Zhang J (2016) Ag-loading on brookite $TiO_2$ quasi nanocubes with exposed {210} and {001} facets: activity and selectivity of $CO_2$ photoreduction to $CO/CH_4$. Appl Catal B-Environ 180:130–138
22. Wei Y, Jiao J, Zhao Z, Liu J, Li J, Jiang G, Wang Y, Duan A (2015) Fabrication of inverse opal $TiO_2$-supported Au@CdS core-shell nanoparticles for efficient photocatalytic $CO_2$ conversion. Appl Catal B-Environ 179:422–432
23. Zhou P, Yu J, Jaroniec M (2014) All-solid-state Z-scheme photocatalytic systems. Adv Mater 26(29):4920–4935
24. Ong WJ, Putri LK, Tan LL, Chai SP, Yong ST (2016) Heterostructured AgX/g-$C_3N_4$ (X=Cl and Br) nanocomposites via a sonication-assisted deposition-precipitation approach: emerging role of halide ions in the synergistic photocatalytic reduction of carbon dioxide. Appl Catal B-Environ 180:530–543
25. He Y, Zhang L, Teng B, Fan M (2015) New application of Z-scheme $Ag_3PO_4$/g-$C_3N_4$ composite in converting $CO_2$ to fuel. Envirom Sci Technol 49(1):649–656
26. Chang X, Wang T, Gong J (2016) $CO_2$ photo-reduction: insights into $CO_2$ activation and reaction on surfaces of photocatalysts. Energy Environ Sci 9:2177–2196
27. Ji Y, Luo Y (2016) New mechanism for photocatalytic reduction of $CO_2$ on the anatase $TiO_2$ (101) surface: the essential role of oxygen vacancy. J Am Chem Soc 138(49):15896–15902
28. Kar P, Farsinezhad S, Mahdi N, Zhang Y, Obuekwe U, Sharma H, Shen J, Semagina N, Shankar K (2016) Enhanced $CH_4$ yield by photocatalytic $CO_2$ reduction using $TiO_2$ nanotube arrays grafted with Au, Ru, and ZnPd nanoparticles. Nano Res 9(11):3478–3493
29. Li M, Li P, Chang K, Wang T, Liu L, Kang Q, Ouyang S, Ye J (2015) Highly efficient and stable photocatalytic reduction of $CO_2$ to $CH_4$ over Ru loaded $NaTaO_3$. Chem Commun (Camb) 51(36):7645–7648
30. Yu B, Zhou Y, Li P, Tu W, Li P, Tang L, Ye J, Zou Z (2016) Photocatalytic reduction of $CO_2$ over Ag/$TiO_2$ nanocomposites prepared with a simple and rapid silver mirror method. Nanoscale 8(23):11870–11874
31. Pan Y, Sun Z, Cong H, Men Y, Xin S, Song J, Yu S (2016) Photocatalytic $CO_2$ reduction highly enhanced by oxygen vacancies on Pt-nanoparticle-dispersed gallium oxide. Nano Res 9 (6):1689–1700
32. Lee S, Jeong S, Kim WD, Lee S, Lee K, Bae WK, Moon JH, Lee S, Lee DC (2016) Low-coordinated surface atoms of CuPt alloy cocatalysts on $TiO_2$ for enhanced photocatalytic conversion of $CO_2$. Nanoscale 8(19):10043–10048
33. Kang Q, Wang T, Li P, Liu L, Chang K, Li M, Ye J (2015) Photocatalytic reduction of carbon dioxide by hydrous hydrazine over Au-Cu alloy nanoparticles supported on $SrTiO_3$/$TiO_2$ coaxial nanotube arrays. Angew Chem Int Ed 54(3):841–845
34. Wang T, Shi L, Tang J, Malgras V, Asahina S, Liu G, Zhang H, Meng X, Chang K, He J, Terasaki O, Yamauchi Y, Ye J (2016) A $Co_3O_4$-embedded porous ZnO rhombic dodecahedron prepared using zeolitic imidazolate frameworks as precursors for $CO_2$ photoreduction. Nanoscale 8(12):6712–6720
35. Wang WN, Wu F, Myung Y et al (2015) Surface engineered CuO nanowires with ZnO islands for $CO_2$ photoreduction. ACS Appl Mater Interfaces 7(10):5685–5692
36. Yu W, Xu D, Peng T (2015) Enhanced photocatalytic activity of g-$C_3N_4$ for selective $CO_2$ reduction to $CH_3OH$ via facile coupling of ZnO: a direct Z-scheme mechanism. J Mater Chem A 3:19936–19947
37. In S-I, Dimitri D, Vaughn II, Schaak RE (2012) Hybrid CuO-$TiO_2$-xNx hollow nanocubes for photocatalytic conversion of $CO_2$ into methane under solar irradiation. Angew Chem Int Ed 124:3981–3984

38. Jin J, Yu J, Guo D, Cui C, Ho W (2015) A hierarchical Z-scheme CdS-$WO_3$ photocatalyst with enhanced $CO_2$ reduction activity. Small 11(39):5262–5271
39. Wang J, Yao H, Fan Z, Zhang L, Wang J, Zang S, Li Z (2016) Indirect Z-scheme BiOI/g-$C_3N_4$ photocatalysts with enhanced photoreduction $CO_2$ activity under visible light irradiation. ACS Appl Mater Interfaces 8(6):3765–3775
40. Li P, Zhou Y, Zhao Z, Xu Q, Wang X, Xiao M, Zou Z (2015) Hexahedron prism-anchored octahedronal $CeO_2$: crystal facet-based homojunction promoting efficient solar fuel synthesis. J Am Chem Soc 137(30):9547–9550
41. Zhai Q, Xie S, Fan W, Zhang Q, Wang Y, Deng W, Wang Y (2013) Photocatalytic conversion of carbon dioxide with water into methane: platinum and copper(I) oxide co-catalysts with a core-shell structure. Angew Chem Int Ed 125(22):5888–5891
42. Liu Q, Zhou Y, Kou J et al (2010) High-yield synthesis of ultralong and ultrathin $Zn_2GeO_4$ nanoribbons toward improved photocatalytic reduction of $CO_2$ into renewable hydrocarbon fuel. J Am Chem Soc 132(41):14385–14387
43. Sarkar A, Gracia-Espino E, Wågberg T, Shchukarev A, Mohl M, Rautio AR, Pitkänen O, Sharifi T, Kordas K, Mikkola JP (2016) Photocatalytic reduction of $CO_2$ with $H_2O$ over modified $TiO_2$ nanofibers: understanding the reduction pathway. Nano Res 9(7):1956–1968
44. Wei Y, Jiao J, Zhao Z, Zhong W, Li J, Liu J, Jiang G, Duan A (2015) 3D ordered macroporous $TiO_2$-supported Pt@CdS core-shell nanoparticles: design, synthesis and efficient photocatalytic conversion of $CO_2$ with water to methane. J Mater Chem A 3(20):11074–11085
45. Li H, Gao Y, Zhou Y et al (2016) Construction and nanoscale detection of interfacial charge transfer of elegant Z-scheme $WO_3$/Au/$In_2S_3$ nanowire arrays. Nano Lett 16(9):5547–5552
46. Pastrana-Martínez LM, Silva AMT, Fonseca NNC, Vaz JR, Figueiredo JL, Faria JL (2016) Photocatalytic reduction of $CO_2$ with water into methanol and ethanol using graphene derivative-$TiO_2$ composites: effect of pH and copper(I) oxide. Top Catal 59(15–16):1279–1291
47. Pan Y, You Y, Xin S, Li Y, Fu G, Cui Z, Men Y, Cao F, Yu S, Goodenough JB (2017) Photocatalytic $CO_2$ reduction by carbon-coated indium-oxide nanobelts. J Am Chem Soc 139 (11):4123–4129
48. Wang Y, Bai X, Qin H, Wang F, Li Y, Li X, Kang S, Zuo Y, Cui L (2016) Facile one-step synthesis of hybrid graphitic carbon nitride and carbon composites as high-performance catalysts for $CO_2$ photocatalytic conversion. ACS Appl Mater Interfaces 8(27):17212–17219
49. Tu W, Zhou Y, Liu Q, Yan S, Bao S, Wang X, Xiao M, Zou Z (2013) An in situ simultaneous reduction-hydrolysis technique for fabrication of $TiO_2$-graphene 2D sandwich-like hybrid nanosheets: graphene-promoted selectivity of photocatalytic-driven hydrogenation and coupling of $CO_2$ into methane and ethane. Adv Funct Mater 23(14):1743–1749
50. Tu W, Zhou Y, Liu Q, Tian Z, Gao J, Chen X, Zhang H, Liu J, Zou Z (2012) Robust hollow spheres consisting of alternating titania nanosheets and graphene nanosheets with high photocatalytic activity for $CO_2$ conversion into renewable fuels. Adv Funct Mater 22 (6):1215–1221
51. Gao C, Meng Q, Zhao K et al (2016) $Co_3O_4$ hexagonal platelets with controllable facets enabling highly efficient visible-light photocatalytic reduction of $CO_2$. Adv Mater 28 (30):6485–6490
52. Xu Y, Yang M, Chen B, Wang X, Chen H, Kuang D, Su C (2017) A $CsPbBr_3$ perovskite quantum dot/graphene oxide composite for photocatalytic $CO_2$ reduction. J Am Chem Soc 139 (16):5660–5663
53. Li R, Hu J, Deng M et al (2014) Integration of an inorganic semiconductor with a metal–organic framework: a platform for enhanced gaseous photocatalytic reactions. Adv Mater 26 (28):4783–4788
54. Yu J, Jin J, Cheng B, Jaroniec M (2014) A noble metal-free reduced graphene oxide–CdS nanorod composite for the enhanced visible-light photocatalytic reduction of $CO_2$ to solar fuel. J Mater Chem A 2(10):3407
55. Ong WJ, Putri LK, Tan YC, Tan LL, Li N, Ng YH, Wen X, Chai SP (2017) Unravelling charge carrier dynamics in protonated g-$C_3N_4$ interfaced with carbon nanodots as co-catalysts toward

enhanced photocatalytic $CO_2$ reduction: a combined experimental and first-principles DFT study. Nano Res 10(5):1673–1696
56. Shi L, Wang T, Zhang H, Chang K, Ye J (2015) Electrostatic self-assembly of nanosized carbon nitride nanosheet onto a zirconium metal-organic framework for enhanced photocatalytic $CO_2$ reduction. Adv Funct Mater 25(33):5360–5367
57. Park SM, Razzaq A, Park YH, Sorcar S, Park Y, Grimes CA, In SI (2016) Hybrid $Cu_xO$-$TiO_2$ heterostructured composites for photocatalytic $CO_2$ reduction into methane using solar irradiation: sunlight into fuel. ACS Omega 1(5):868–875
58. Ong WJ, Tan LL, Chai SP, Yong ST, Mohamed AR (2015) Surface charge modification via protonation of graphitic carbon nitride (g-$C_3N_4$) for electrostatic self-assembly construction of 2D/2D reduced graphene oxide (rGO)/g-$C_3N_4$ nanostructures toward enhanced photocatalytic reduction of carbon dioxide to methane. Nano Energy 13:757–770
59. Ming H, Ma Z, Liu Y, Pan K, Yu H, Wang F, Kang Z (2012) Large scale electrochemical synthesis of high quality carbon nanodots and their photocatalytic property. Dalton Trans 41 (31):9526–9531
60. Yu H, Zhao Y, Zhou C, Shang L, Peng Y, Cao Y, Wu L, Tung C, Zhang T (2014) Carbon quantum dots/$TiO_2$ composites for efficient photocatalytic hydrogen evolution. J Mater Chem A 2(10):3344
61. Shi H, Chen G, Zhang C, Zou Z (2014) Polymeric g-$C_3N_4$ coupled with $NaNbO_3$ nanowires toward enhanced photocatalytic reduction of $CO_2$ into renewable fuel. ACS Catal 4 (10):3637–3643
62. Wang D, Hisatomi T, Takata T, Pan C, Katayama M, Kubota J, Domen K (2013) Core/Shell photocatalyst with spatially separated co-catalysts for efficient reduction and oxidation of water. Angew Chem Int Ed 52(43):11252–11256
63. Zheng D, Cao X, Wang X (2016) Precise formation of a hollow carbon nitride structure with a janus surface to promote water splitting by photoredox catalysis. Angew Chem Int Ed 55 (38):11512–11516
64. Li A, Chang X, Huang Z et al (2016) Thin heterojunctions and spatially separated cocatalysts to simultaneously reduce bulk and surface recombination in photocatalysts. Angew Chem Int Ed 55(44):13734–13738
65. Zhang J, Yu Z, Gao Z, Ge H, Zhao S, Chen C, Chen S, Tong X, Wang M, Zheng Z, Qin Y (2017) Porous $TiO_2$ nanotubes with spatially separated platinum and $CoO_x$ cocatalysts produced by atomic layer deposition for photocatalytic hydrogen production. Angew Chem Int Ed Eng 56(3):816–820
66. Xie S, Wang Y, Zhang Q, Fan W, Deng W, Wang Y (2013) Photocatalytic reduction of $CO_2$ with $H_2O$: significant enhancement of the activity of Pt-$TiO_2$ in $CH_4$ formation by addition of MgO. Chem Commun (Camb) 49(24):2451–2453
67. Mistry H, Varela AS, Kühl S, Strasser P, Cuenya BR (2016) Nanostructured electrocatalysts with tunable activity and selectivity. Nat Rev Mater 1(4):16009
68. Gao D, Zhou H, Wang J, Miao S, Yang F, Wang G, Wang J, Bao X (2015) Size-dependent electrocatalytic reduction of $CO_2$ over Pd nanoparticles. J Am Chem Soc 137(13):4288–4291
69. Gao G, Jiao Y, Waclawik ER, Du A (2016) Single atom (Pd/Pt) supported on graphitic carbon nitride as an efficient photocatalyst for visible-light reduction of carbon dioxide. J Am Chem Soc 138(19):6292–6297